universität wien

MASTERARBEIT / MASTER'S THESIS

Titel der Masterarbeit / Title of the Master's Thesis

„Strain-dependent microfabric evolution of experimentally deformed synthetic eclogites“

verfasst von / submitted by

Pt. Philipp Christos Julian Thospann

angestrebter akademischer Grad / in partial fulfilment of the requirements for the degree of

Master of Science (MSc)

Wien, 2023 / Vienna 2023

Studienkennzahl lt. Studienblatt / degree programme code as it appears on the student record sheet:	UA 066 815
Studienrichtung lt. Studienblatt / degree programme as it appears on the student record sheet:	Masterstudium Erdwissenschaften
Betreut von / Supervisor:	Univ. Prof. Dr. Mag. Bernhard Grasemann

ACKNOWLEDGMENTS

I would like to express my sincere gratitude to my thesis supervisor, Anna Rogowitz, for her patience and support throughout these years. Her research ideas, constructive feedback, and detailed explanations have been invaluable to the development of my thesis. I am also grateful to her for conducting the electron microscope analyses alongside me.
I extend my appreciation to Sarah Incel, who provided supervision during my experiments and performed the sample synthesis, and to Florian Fusseis for his supervision and support in the 3D analyses.
My heartfelt thanks also go to Ian Butler for performing the X-ray microtomography scanning, to Ilka Wünsche for her meticulous preparation of the thin sections, and to Katrin Kraus for preparing the starting material and generously providing me with data from her study.

This study was financed by the Austrian Science Fund (FWF): Grant number: P 29539 (granted to AR).

ABSTRACT

Deformed eclogites often reveal interconnected layers of omphacite and intercalated elongated garnet clusters. The evolution of such fabrics is usually associated with strain localization and rheological weakening. To provide insights on the development of these fabrics in eclogite, the strain-dependence of deformation mechanisms and microfabrics in omphacite-garnet aggregates was experimentally investigated. Eclogites were synthesized by hot-pressing omphacite-garnet powders (with a volume fraction of 25% garnet) in a piston-cylinder press at 3 GPa and 1100° C for 24 h. These synthetic eclogites were then axially shortened by approximately 4.7%, 7%, and 42% in a Griggs-type deformation apparatus at 2.5 GPa, 900° C, and a strain rate of $6.4 \cdot 10^{-6}$ s^{-1}. The low- and moderate-strain experiments documented microstructures developing near the material's yield point and the point of maximum compressive strength, respectively. The recovered samples were analyzed by combining x-ray microtomography, optical microscopy and scanning electron microscopy to identify the dominant deformation mechanisms at varying degrees of strain and link them to the microfabrics. Similar to naturally deformed eclogites, strain partitioning was observed in the experimental samples, where the omphacite matrix accommodated most of the strain while garnet grains essentially behaved like rigid bodies. Stress concentrated at narrow omphacite-rich zones situated in between garnet clusters and at garnet-garnet contacts, promoting strain localization. At low to moderate strains, omphacite exhibits a weak shape preferred orientation and garnet tends to initialize cluster formation. The highly strained sample displays a fully developed S-type foliation, with elongated omphacite crystals and garnet clusters both exhibiting a pronounced shape preferred orientation. Foliation development segregated garnet clusters into distinct layers perpendicular to the maximum compressive stress, resulting in a decrease in garnet's three-dimensional interconnectivity. A reduction in grain size and an increase in density of low-angle grain boundaries with increasing strain indicates crystal-plastic deformation of omphacite by dislocation creep. The thinned out, elongated garnet clusters are due to cataclasis, as indicated by brittle deformation in the form of micro-cracking. Evidence for minor crystal-plastic deformation of garnet occurs locally in the vicinity of fractured garnet-garnet contacts, where high differential stresses localized, resulting in increased misorientation.

SUMMARY IN GERMAN LANGUAGE (ZUSAMMENFASSUNG)

Deformierte Eklogite bestehen häufig aus vernetzten Omphazitschichten und eingelagerten elongierten Granatclustern. Die Entwicklung solcher Gefüge ist in der Regel mit Strain-Lokalisierung und rheologischer Abschwächung verbunden. Um Einblicke in die Entwicklung dieser Gefüge in Eklogiten zu verschaffen, wurde die Strain-Abhängigkeit von Deformationsmechanismen und Mikrogefügen in Omphazit-Granat-Aggregaten experimentell untersucht. Eklogite wurden durch Heißpressen von Omphazit-Granat-Pulvern (mit einem Volumenanteil von 25% Granat) in einer Kolben-Zylinder-Presse bei 3 GPa und 1100 °C für 24 Stunden synthetisiert. Diese synthetischen Eklogite wurden dann in einem Griggs-Typ-Deformationsapparat bei 2.5 GPa, 900 °C und einer Strainrate von $6.4 \cdot 10^{-6}$ s^{-1} axial um etwa 4.7%, 7% und 42% verkürzt. Die Experimente mit geringer bzw. mäßiger Deformation dokumentierten Mikrostrukturen, die sich in der Nähe des Yield-Punktes bzw. des Punktes maximaler Druckfestigkeit des Materials entwickelten. Die deformierten Proben wurden mittels Kombination von Röntgenmikrotomographie, optischer Mikroskopie und Rasterelektronenmikroskopie analysiert, um die dominierenden Deformationsmechanismen bei unterschiedlichen Strain-Graden zu identifizieren und sie mit den Mikrogefügen in Verbindung zu bringen. Ähnlich wie bei natürlich deformierten Eklogiten wurde in den experimentellen Proben eine Strain-Partitionierung beobachtet, in welcher die Omphazit-Matrix den Großteil der Deformation aufnahm, während sich die Granatkörner im Wesentlichen wie starre Körper verhielten. Die Spannung konzentrierte sich auf schmale, omphazitreiche Zonen zwischen den Granatclustern und an den Granat-Granat-Kontakten, was die Lokalisierung von Strain förderte. Bei geringer bis mäßiger Deformation weist der Omphazit eine schwache Formvorzugsorientierung der Körner auf und der Granat neigt dazu, die Clusterbildung zu initiieren. Bei der stark deformierten Probe bildete sich eine voll entwickelte S-Typ-Foliation, wobei sowohl elongierte Omphazitkristallen als auch Granatcluster eine ausgeprägte Formvorzugsorientierung aufweisen. Die Entwicklung der Foliation separierte die Granatcluster in deutlichen Schichten senkrecht zur maximalen Druckspannung, was zu einer Abnahme der dreidimensionalen Vernetzbarkeit des Granats führte. Eine Verringerung der Korngröße und eine Zunahme der Dichte von Kleinwinkel-Korngrenzen mit zunehmender Deformation deuten auf eine Kristallplastizität von Omphazit durch Dislokationskriechen hin. Die ausgedünnten, elongierten Granatcluster sind auf Kataklase zurückzuführen, die sich durch spröde Deformation in Form von Mikrorissen erkennen lässt. Anzeichen für eine geringfügige Kristallplastizität von Granat treten lokal in der Nähe von gebrochenen Granat-Granat-Kontakten auf, wo hohe differentielle Spannungen lokalisierten, was zu einer erhöhten Missorientierung führte.

TABLE OF CONTENTS

LIST OF ABBREVIATIONS

2D: Two dimensions

3D: Three dimensions

CPO: Crystallographic preferred orientation

EDX: Energy dispersive x-ray

FSD: Forward scattered detector

Grt: Garnet

HP/HT: High pressure/high temperature

IWL: Interconnected weak layer

Jd-Dio: Jadeite-diopside

LBF: Load-bearing framework

LVDT: Linear variable displacement transducer

Micro CT: Micro-(computer)-tomography

OC: Orientation contrast

Omp: Omphacite

P/T: Pressure/temperature

SEM: Scanning electron microscopy

SLD: Star length distribution

SPO: Shape preferred orientation

SVD: Star volume distribution

UHP: Ultra-high pressure

VOI: Volume of interest

WR: Whole rock

1. INTRODUCTION

1.1. Eclogite – the Chosen One

Eclogites were first described in 1822 by René Just Haüy, a French mineralogist who examined them at the Saualpe in Austria. He was impressed by their unusual beauty and named them "chosen rocks", a name he derived from the Greek word "εκλογή" ("ek-lo-ghi"), meaning "choice". Although eclogites are rarely found at the Earth's surface, they highly impacted several geologic concepts in geodynamics and metamorphic petrology.

Eclogites are high-pressure (HP) to ultra-high pressure (UHP) metamorphic rocks composed primarily of two phases (≥ 75% vol.): garnet, usually with a Mg-rich (almandine) or Fe-rich (pyrope) composition, and omphacite (clinopyroxene), usually with a Na-rich (jadeite) or Ca-Mg-rich (diopside) composition. Eclogites have a relatively high bulk density, ranging from 3.2 to 4.1 g/cm^3 (e.g. Ji et al., 2003), which indicates that very high pressures were involved in their formation. Accessory minerals typically found in eclogites include quartz, kyanite, mica, rutile, and pyroxenes, sometimes amphiboles, epidote, zoisite, titanite, lawsonite, and rarely the UHP minerals coesite, corundum, and diamond.

Occurrences of eclogites at the surface are rare, typically found within peridotite bodies or as xenoliths in kimberlitic intrusions (mantle eclogites), as bands or lenses within glaucophane schists (ophiolitic eclogites), and within gneiss and migmatite (orogenic eclogites) (Smulikowski, 1964; Coleman et al., 1965). Eclogites are responsible for naming a type of metamorphic facies; the eclogite facies are characterized by pressures exceeding 1.2 GPa (~45 km depth) and temperatures of at least 400 – 500° C. Most eclogites are formed under low thermal gradients in subduction zones through the metamorphism of dry mafic rocks with basaltic composition (i.e. basalt, gabbro, granulite) (Green & Ringwood, 1967). Unlike their protoliths, eclogites don't contain plagioclase. The metasedimentary counterparts of eclogites are schists and gneisses.

1.2. Geodynamic Significance of Eclogites

Eclogites constitute a significant volume of the Earth's lower crust and upper mantle; they play a crucial role in the deformation of the lower lithosphere, as well as the heat and mass transfer within the Earth. The density and rheological contrast between eclogites and their neighboring rocks influence various lithospheric processes at converging plate boundaries, including both subduction zones (e.g. Agard et al., 2018, 2020) and collision zones (e.g. Austrheim, 2013). Rheological processes, such as the strain localization and rheological weakening of eclogites are potential driving forces for the initiation of oceanic lithosphere subduction (e.g. Stern & Gerya, 2018), the initiation of intracontinental subduction (e.g. Hacker et al., 2015; Miladinova et al., 2021), the delamination of both oceanic and continental lithosphere (e.g. Bird, 1979; Philippot & van Roermund, 1992; Li et al., 2016), and the exhumation of high-pressure (and UHP) terrains (e.g. Jolivet et al., 2005; Burov et al, 2014). Furthermore, the process of eclogitization and associated dehydration has been linked to mechanisms of intermediate and deep earthquake generation (e.g. Austrheim & Boundy, 1994; Kirby et al., 1996; Hacker et al., 2003; Zhang et al., 2004).

1.3. The Study of Eclogite Rheology

Studying the rheology of lower lithosphere rocks, particularly eclogites, poses a key challenge. The fact that their deformation occurs deep within the Earth, makes it impossible to directly observe and measure their flow behavior. Nevertheless, it has been shown that the microfabric of experimentally deformed rocks, including eclogites, is comparable to the microfabric of naturally deformed rocks, permitting the extrapolation of mechanical data from deformation experiments to natural conditions (e.g. Zhang & Green, 2007). These experiments simulate the pressure/temperature (P/T) conditions prevalent in the lower lithosphere and incorporate strain rates that can be extrapolated to geological timescales. To increase the flexibility of deformation experiments, synthetic rock samples are often utilized (e.g. Zhang & Green, 2007; Rogowitz et al., 2023). Unlike natural samples, they allow researchers to control intrinsic conditions, such as the water content, grain size, and volume fractions of the primary phases. The mechanical data obtained from deformation experiments are utilized to quantitatively associate microfabrics and deformation mechanisms with deformation conditions (e.g. Zhang & Green, 2007), to determine flow laws of single- and polyphase aggregates (e.g. Zhang & Green, 2007), and to evaluate the accuracy of mixing models (e.g. Huet et al., 2014). Mixing models and numerical simulations also facilitate the determination of flow laws (e.g. Huet et al., 2014; Rast & Ruh, 2021). Moreover, numerical simulations are employed to model deformation behavior under diverse sets of conditions (e.g. Yamato et al., 2019; Rogowitz et al., 2023).

1.4. Motivation and Scope

The study of eclogite rheology is a multifaceted and ongoing field that requires integration of various disciplines and techniques. A comprehensive understanding of eclogite deformation can offer vital insights into a variety of lithospheric processes at convergent plate boundaries. However, the association between strain and the dominant deformation mechanisms remains unclear, particularly in the low strain domain, where the onset of foliation development is believed to occur. This study aims to provide constraints on the effect of strain on the microfabric, microstructures, and deformation mechanisms of experimentally deformed synthetic dry eclogite samples.

Four dry eclogite samples (omphacite-garnet aggregates) were synthesized with a composition of 75% omphacite – 25% garnet. Three samples were deformed to varying degrees of strain using a Griggs-type deformation apparatus at 2.5 GPa confining pressure, 900° C temperature, and $6.4 \cdot 10^{-6}$ s^{-1} strain rate. Previous experiments employing similar samples have demonstrated that the implemented conditions consistently produce prominent foliation microfabrics (Rogowitz, et al., 2023; Kraus, K. (unpublished)).

The microfabrics of the experimental samples were examined by performing a series of microstructural analyses both in two dimensions (2D) and in three dimensions (3D). The 2D analyses included optical microscopy and scanning electron microscopy (SEM); the latter provided qualitative z-contrast and orientation contrast (OC) data, used to identify the dominant deformation mechanisms. The 3D analyses were performed using an x-ray microtomography instrument (micro CT) to quantitatively assess the 3D interconnectivity of garnet and the 3D shapes of both primary phases at different degrees of strain.

2. RHEOLOGY

2.1. Flow Behavior of Polymineralic Rocks

The rheology of polymineralic rocks is a complex and multifaceted subject that depends on a range of intrinsic and extrinsic factors. Intrinsic properties, such as the flow parameters, volume fractions, grain size, chemical properties, and competence contrast of their major constituents, as well as the overall microstructural characteristics and the fluid content, all influence their deformation behavior. Meanwhile, extrinsic conditions, such as the confining pressure, temperature, strain rate, and accumulated strain all have a significant impact on their rheological response to imposed stress.

2.1.1. A Mechanical and Microstructural Model

The bulk strength of polymineralic heterogeneous rocks typically falls between the strengths of their weakest and strongest primary mineral phases. Although strength generally increases with a higher content of the more competent minerals, this correlation is highly nonlinear. Early deformation experiments conducted on two-phase aggregates revealed that their overall strength is disproportionately influenced by the weaker phase (e.g. Jordan 1987), and similar observations have been made in naturally deformed rocks (e.g. Schulmann et al., 1996). The bulk strength of polymineralic rocks depends on the intensity of stress and strain rate partitioning, which is a function of temperature, bulk strain rate, and the flow parameters and volume fractions of the major constituents (Handy, 1990).

Handy (1990) conceptualized a widely adopted mechanical/microstructural model to account for stress and strain rate partitioning in polymineralic rocks. It describes three end-members, characterized by the competence contrast and volume fraction of the primary phases. The load-bearing framework (LBF) is a clast-supported microstructure, in which strong phases dominate the rheology. The others are matrix-supported – characterized by an interconnected weak layer (IWL), namely the clast-matrix, where the weak phases dominate the rheology, and the boudin-matrix, in which all major phases jointly govern the rheology.

The LBF refers mainly to rocks with low proportions of weak phases (< 30%). It applies to a minor volume of lower crust/upper mantle rocks (e.g. pyroxenites, diorites). The LBF is characterized by a stress-supporting, interconnected framework composed of strong phases; the weaker phases are confined within isolated pockets. Strain rate is nearly uniformly distributed in LBF aggregates, and their bulk strength is highly dependent on the strong phases' strength, as well as the size, shape, and distribution of the weaker phases. IWL rheologies are much more common than LBF. The IWL clast-matrix microstructure applies to most quartz-rich rocks (e.g. granites and granodiorites at 200 – 800° C), salts, hydrous sulphates, and carbonates with a high competence contrast (≥ 10: 1). It exhibits significant stress/strain partitioning as strong phases remain relatively undeformed within the highly strained, interconnected matrix. The boudin-matrix refers to rocks with a low competence contrast (≤ 10: 1), such as some silicates in the lower crust or within ultramylonitic shear zones. It is characterized by elongated boudins of strong phases within a weaker interconnected matrix; both the weak and strong phases are rheologically active.

The diagram in Figure 1 (slightly modified after Handy, 1990), depicts normalized aggregate strength versus weak phase volume fraction. Three domains represent the three rheological end-members: domain 1 is the LBF, domain 2 is the boudin-matrix (IWL), and domain 3 is the clast-matrix (IWL). Normalized strength is defined as the ratio of bulk strength to the strength of strong phases. The right hand axis depicts the strength ratio, which is the ratio between the strength of strong phases to the strength of weak phases (competence contrast). The thin contours depict trajectories of normalized strength with variable weak phase volume fractions at a constant strength ratio. The negative slope and upwards concave shape of the contours indicate the higher influence of strong phases on the bulk strength at high strong phase volumes, and particularly at higher strength ratios. The mechanical boundary between the clast-matrix and the boudin-matrix domain is diffuse, indicating a high dependence on the competence contrast and shape/spatial distribution of the main phases to induce the onset of yielding of strong phases. The change in slope of the contours of constant strength ratio at the boundary between domain 2 and 3 reflects the differences in strain partitioning between the two IWL rheologies. The mechanical boundary separating the LBF from the IWL domains is sharp, and the contours' slopes at the boundary change drastically, indicating the great influence strong phases exert on the bulk strength of LBF aggregates.

For a given competence contrast (thin contours), for instance 10: 1, aggregates remain in the IWL clast-matrix domain for volume fractions of the strong phases up to 70%. The overall strength approximates that of the pure weaker phases. Beyond 70%, aggregates enter the LBF domain, and a sudden increase in the overall strength occurs. The abundance of strong phase clasts, combined with their size/shape, results in interconnectivity between them; the interconnected strong phases are capable of supporting the imposed stress. Further increase in strong phase content leads to the bulk aggregate strength approximating that of the pure strong phases.

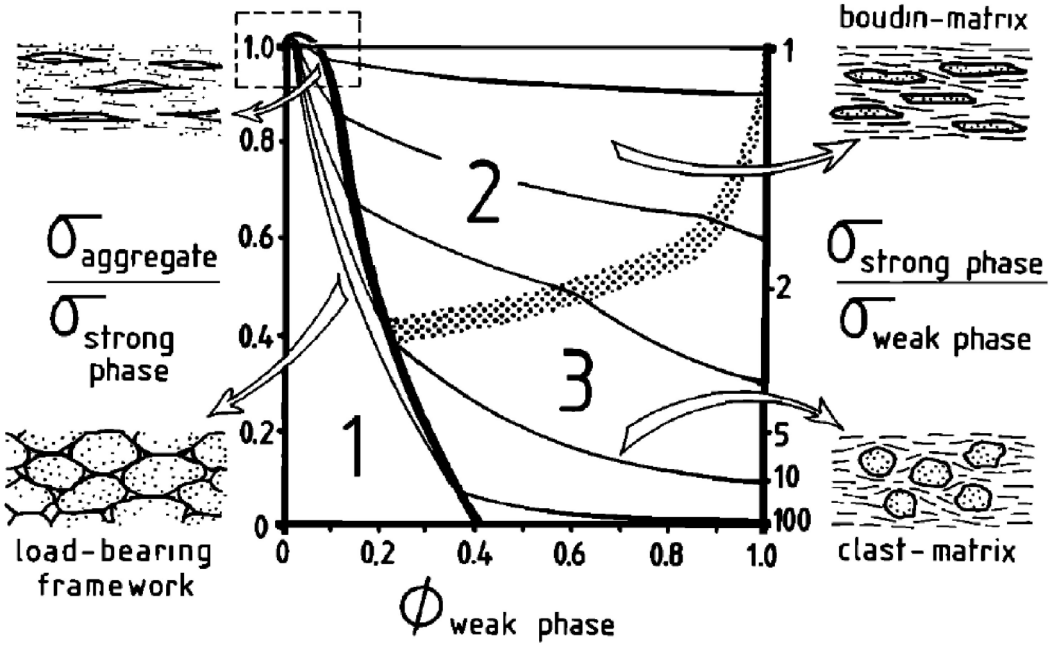

Figure 1: Normalized strength vs weak phase volume fraction and characteristic microstructures. Domain 1: Load bearing framework. Domain 2: Boudin-matrix (IWL). Domain 3: clast-matrix (IWL). The border between domain 1 and the other two is sharp (bold curve), the border between domains 2 and 3 is diffuse (dotted). The right hand axis depicts the strength ratio. Thin contours depict trajectories of constant strength ratio (slightly modified after Handy, 1990).

2.1.2. Extrinsic Factors

The competence contrast of polymineralic heterogeneous rocks may change or even reverse according to alterations in extrinsic conditions, particularly strain, strain rate and temperature. The accumulation of strain results to shifting of the mechanical boundaries (white arrows in Figure 2: modified after Handy, 1990). An LBF aggregate typically transitions to an IWL rheology since even low strains could induce a collapse of the framework and interconnection of the isolated pockets containing weak phases, leading to foliation development and strength reduction (Jordan, 1988). Consequently, the boundary between the LBF and the IWL rheologies shifts towards lower bulk strengths and lower weak phase volumes. An aggregate characterized by a clast-matrix IWL rheology typically transitions to a boudin-matrix IWL rheology, indicated by yielding of the clasts (Handy, 1990). The boundary between the two IWL domains and the contours both shift towards lower bulk strengths, as the strong phases progressively yield at higher strength ratios. In cases of very high strain, the competence contrast can be reduced dramatically, resulting in rheologically homogeneous aggregates, as has been observed in mylonites (e.g. Schulmann et al., 1996).

Variations in strain rate and temperature exert significant influence on the competence contrast between the major phases, resulting in an upward/downward shifting of the plotted position of a deforming aggregate with respect to the contours (black arrows in Figure 2: modified after Handy, 1990). While the strength ratio of IWL rheologies typically reduces in response to either elevated temperatures or strain rates, the strength ratio of LBF rheologies reduces at higher temperatures but increases at higher strain rates and (Handy, 1990). Increased temperatures or lower strain rates reduce stress concentrations in the neck regions of an LBF aggregate, reducing its strength ratio and increasing its bulk strength. The strength ratio reduction of polymineralic aggregates can be very drastic, in extreme cases resulting even in an inversion. For example, the rheology of feldspar-pyroxene aggregates (gabbro) is dominated by the volume fraction of feldspar, which below 900° C is the weaker phase (IWL). At higher temperatures, pyroxene becomes weaker than feldspar, resulting in a reverse in competence contrast (Blenkinsop, 2000).

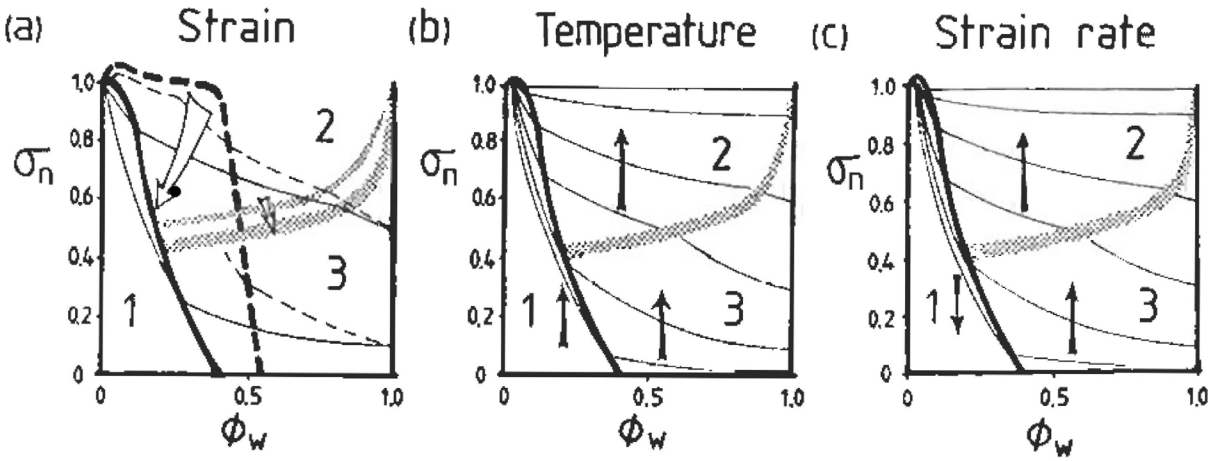

Figure 2: Normalized strength vs weak phase volume fraction. Subfigure (a) shows the effect of imposed strain on the boundaries of the rheological domains. Subfigure (b) shows the effect of increasing temperature on the strength ratio. Subfigure (c) shows the effect of increasing strain rates on the strength ratio. White arrows in (a) indicate the mechanical boundary shifting direction with increase of imposed conditions. Black arrows in (b) and (c) indicate the competence contrast shift of aggregates with increasing imposed conditions (modified after Handy, 1990).

Pressure is usually considered to have minor influence on the competence contrast since creep mechanisms are typically more sensitive to variations in temperature and strain rate. However, in fluid-rich conditions, an increase in pore pressure can induce brittle failure and thus reduce bulk strength (e.g. Rutter, 1972). Moreover, syntectonic alterations in temperature, pressure, or fluid content often affect mineral stability. Mineral reactions can exert drastic effects on the rheology, often resulting in bulk strength reduction (Handy, 1990).

2.1.3. Foliation Weakening Mechanisms

Strain weakening is the process of reduction in a rock's bulk strength due to increasing strain. It is typically associated with foliation development and often results in strain localized zones, commonly referred to as shear zones. Strain weakening of an aggregate occurs due to the dissipation of stress concentrations, causing less strain energy to be expended for each incremental increase in strain (Handy, 1990). Stress concentrations within the matrix are promoted by a high competence contrast (Kenkmann & Dresen, 1998), large clast size and limited average clast spacing (Handy, 1990).

Foliation development substantially contributes to the weakening of IWL aggregates by reducing clast size, increasing average clast spacing, and enhancing matrix interconnectivity (Handy, 1990). This process dissipates stress concentrations in the matrix, as it increases the matrix surface area available for absorbing strain energy, enabling weaker phases to exert a disproportionate influence on the aggregate's bulk strength. The weakening effect of foliation is more pronounced at lower volumes of weaker phases (Handy, 1990).

Dissipation of stress concentrations occurs through small-scale processes that typically operate during foliation development. Stress concentrations cause strong phases to yield through cataclasis or plastic flow, reducing their average grain size and dissipating stress concentrations. However, the amount of strain weakening resulting from clast-related stress dissipation is minor compared to matrix-related weakening (Handy, 1990). Stress concentrations in the matrix are typically dissipated through grain size reduction via dynamic recrystallization, which alone can result in a significant reduction in matrix flow strength if it's enhanced by cataclasis or syntectonic reactions, or if crystal growth is inhibited (De Bresser et al., 2001). Grain size reduction often triggers a switch in the operative deformation mechanism from dislocation creep to diffusion creep, leading to further reduction in flow strength (Tasaka et al., 2017).

2.1.4. Flow Laws for Polymineralic Rocks

Modeling of lithospheric processes requires a comprehensive understanding of the flow behavior of polymineralic rocks. Historically, numerical models approximated lithospheric domains using single-phase flow laws, leading to significant errors as rock rheology is typically controlled by multiple phases (e.g., Chen and Molnar, 1983). Deformation experiments on single-phase aggregates are conducted to determine the flow parameters of individual phases, which are then extrapolated to natural conditions (e.g. Moghadam et al., 2010). Similar experiments, as well as numerical methods, are used to determine the bulk flow parameters of two-phase aggregates and their compositional variations (e.g. Zhang & Green, 2007; Rast &

Ruh, 2021). Such two-phase flow laws are a better approximation than single-phase flow laws; however, available experimental data on two-phase aggregates are limited in comparison to the natural diversity of rocks. To overcome this issue, several empirical and analytical models have been developed to derive two- and polyphase flow laws.

The flow properties of polymineralic rocks inherently depend on the individual flow parameters, volume fractions, and microstructures of their major constituents. Due to the distinct and frequently complex microstructures of polymineralic rocks, the majority of current models rely solely on weighting the individual flow properties of the constitutive phases according to their volume fractions. These models are essentially mixing models between two extreme viscosity boundaries: uniformly distributed stress concentrations (Reuss, 1929) or uniformly distributed strain rates (Voigt, 1928). Although all mixing models are founded on numerous assumptions and thus offer approximations with restricted applicability, more recent models present fewer limitations and yield improved approximations of polymineralic rock rheology. However, significant discrepancies among the mixing models suggest that additional research is vital to accurately predict polyphase flow laws. The following presents a review of the most notable mixing models.

Tullis et al. (1991) developed an empirical mixing model that computes the creep strength of two-phase aggregates by weighting the individual dislocation creep flow parameters of each phase by their volume fractions. Although it assumes that the rheology of two-phase aggregates follows a simple power law behavior, it offers a reasonable approximation for rocks with a relatively low competence contrast. Tullis et al. (1991) also developed a finite element numerical method to account for the microstructural complexity of two-phase aggregates; however, this method is too time consuming to be employed on each two-phase aggregate. Handy (1994) developed a more fundamental, analytical approach which addresses the microstructures related to strain partitioning in idealized LBF/IWL two-phase aggregates. The mixing model is based on the principle of strain energy minimization, and has two branches, one for LBF and one for IWL rheologies. Both functions weight the creep strength of the weak and strong phase by their respective volume fractions to compute the creep strength in terms of temperature and strain rate.

The mixing models by Handy (1994) and Tullis et al. (1991) are both designed exclusively for two-phase aggregates deforming through steady state dislocation creep. A generalization to aggregates consisting of more than two major phases was developed by Ji et al. (2003). The mixing model computes flow parameters of polyphase aggregates while addressing for both steady state diffusion creep and dislocation creep. However, the model is based on an iterative process and is limited to coarse grained rocks. A more recent analytical approach by Huet et al. (2014), is based on Handy's (1994) principle of strain energy minimization, and computes the creep strength of polyphase rocks, as well as the stress and strain rate within the constitutive phases. Although its applicability is limited to scales where anisotropies and heterogeneities are negligible, and it assumes steady state flow by dislocation creep, it provides fast, accurate and flexible fit to experimental data. It is crucial to note that all mixing models discussed above describe the bulk viscous flow of aggregates, rather than local internal behavior at the grain scale, as they do not satisfy the stress and strain continuity equations at the interfaces between grains of different phases.

2.2. Eclogite Rheology

2.2.1. Deformation Regime

Eclogites are two-phase, rheologically heterogeneous rocks; thus, their flow behavior is highly dependent on the interactions that arise due to the high competence contrast between garnet and omphacite. Their overall deformation regime, strength, fabric, deformation mechanisms and microstructures vary depending on several factors, such as the P/T conditions of deformation, strain rate, the volume fraction of their major constituents, and the abundance of fluid phases. In most cases, when the deformation conditions are moderate, fluids are sparse, and the garnet content is not very high, their overall deformation behavior is ductile as strain is predominantly accommodated by the creeping omphacite and quartz matrix, while garnet grains behave as rigid inclusions (IWL). This strain partitioning has been observed in both natural eclogites (e.g. Piepenbreier & Stöckhert, 2001; Kurz et al., 2004; Keppler et al., 2016) and in experimental samples (e.g. Jin et al., 2001; Zhang & Green, 2007; Rogowitz et al., 2023). Brittle deformation has also been reported in naturally deformed eclogites and was previously attributed either to seismic strain rates (e.g. Angiboust et al. 2011; Broadwell et al., 2019), or to strain localization due to lithological heterogeneities, or fluid influence (e.g. Hertgen et al., 2017). Moreover, Zhang et al. (2004) demonstrated that eclogites could exhibit brittle failure at high temperatures due to hydroxyl release from omphacite. Even small amounts of water induce melting at grain boundaries and could trigger high-pressure faulting in eclogite (dehydration embrittlement); this mechanism potentially explains deep- and intermediate focus earthquakes. On the other hand, recent experimental studies have demonstrated that eclogites could exhibit brittle failure in the absence of seismic strain rates or fluids. Numerical simulations have shown that increasing strain rates (non-seismic), could induce whole rock (WR) fracturing in eclogites (Figure 3: Yamato et al., 2019). Experiments by Rogowitz et al. (2023) concluded that an increase in garnet content from 50% to 75% (LBF), switches the deformation regime of dry eclogites from crystal-plastic to brittle.

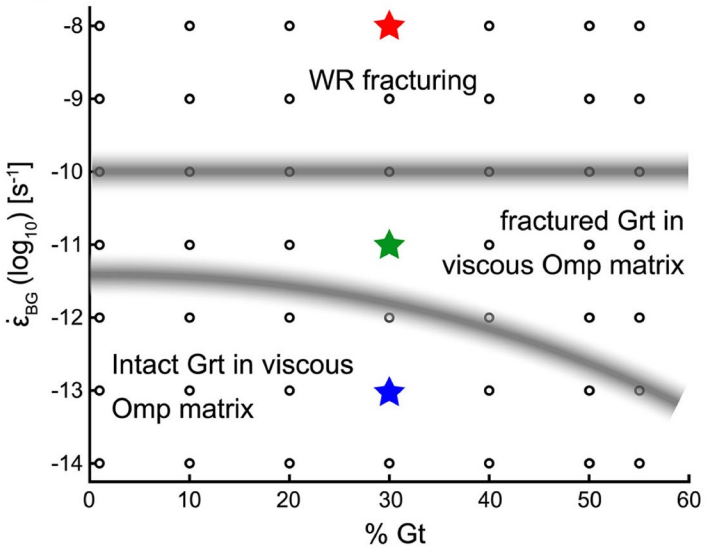

Figure 3: Results from numerical simulations at 2 GPa and 550° C, illustrating the deformation regime transition of eclogites from ductile (viscous), to semibrittle, and finally brittle with increasing strain rates ($\dot{\varepsilon}_{BG}$). Increasing garnet content broadens the semibrittle field towards lower strain rates (Yamato et al., 2019).

2.2.2. Strength

The creep strength of eclogites is comparable to that of harzburgite (Jin et al., 2001; Zhang & Green, 2007), although it strongly depends on the garnet content (Figure 4: Rogowitz et al., 2023; Jin et al., 2001; Zhang & Green, 2007), and water content (Zhang & Green, 2007). Dry eclogites are generally 2 – 3 times stronger than omphacite and ½ as strong as garnet (Zhang & Green, 2007). A typical rheological behavior of eclogites is strain weakening and strain localization in omphacite-rich domains (see Subsection 2.2.5) (e.g. Rogowitz & Huet, 2021; Rogowitz et al., 2023).

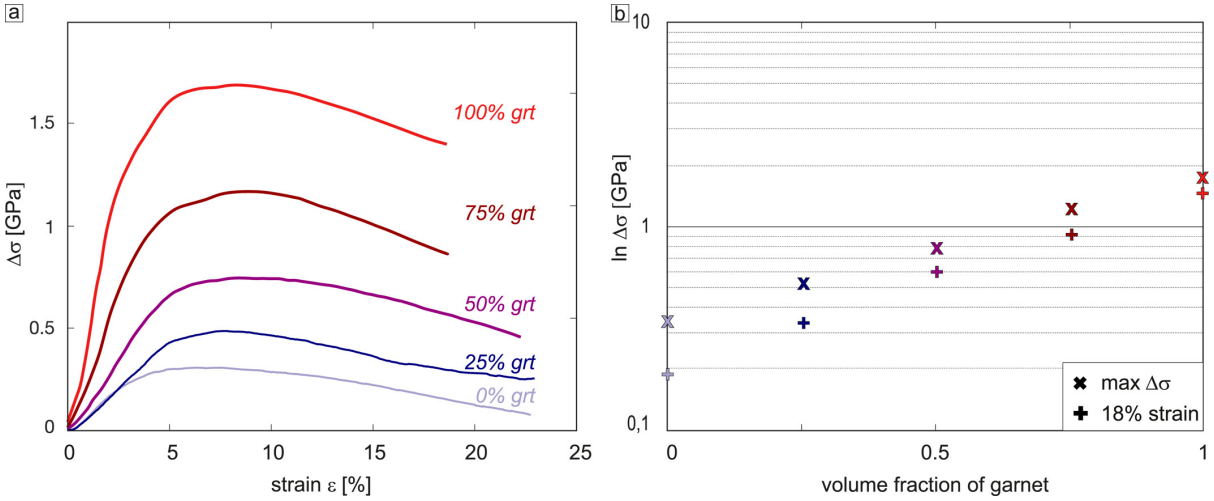

Figure 4: Results from axial compression experiments on dry synthetic eclogites at 2.5 GPa, 1000° C, $3 \cdot 10^{-6}$ s^{-1}. Subfigure (a) shows the derived differential stress-strain curves for samples with various garnet volume fractions. The stress-strain curves illustrate the evolution of differential stress ($\Delta\sigma$), which is equivalent to the compressive strength of the material, with increasing strain (ε). All samples exhibit an initial linear increase in compressive strength (elastic deformation), which is amplified with increasing garnet content. As deformation progresses, samples reach the yield point, where their compressive strength increase begins deviating from a linear correlation with strain. The yield strength of the samples was reached upon accumulating 3 – 5% strain. Further deformation brings samples to their maximum compressive strength ($\Delta\sigma_{max}$), where their strength remains roughly constant for about ~5% strain (steady-state flow). Deformation beyond $\Delta\sigma_{max}$, results in a state of rheological (strain) weakening, where the compressive strength reduces with increasing strain. Strain weakening of eclogites is discussed in more detail in Subsection 2.2.5. Subfigure (b) reveals a positive log-linear correlation between the maximum differential stress ($\Delta\sigma_{max}$), and the volume fraction of garnet. A positive correlation between the intensity of strain weakening and the volume fraction of garnet is also shown (see Subsection 2.2.5). The figure is taken from Rogowitz et al. (2023).

2.2.3. Fabric and Texture

Deformed eclogites commonly develop a foliation and/or lineation, varying between L- and S- type fabrics. Texture is typically characterized by a crystallographic preferred orientation (CPO) and shape preferred orientation (SPO) of omphacite. In high-grade tectonic settings, or when fluids are abundant, garnet also contributes to the foliation by developing an SPO. A layering of garnet and omphacite is commonly observed on the microscopic scale under high strain, revealing extensive clustering of garnet grains. On the mesoscopic scale, eclogites often exhibit a broad range of compositional heterogeneities, arranged spatially in distinct or gradually transitioning layers, or in distinct blocks (e.g. Ji et al., 2003; Kurz et al., 2004; Terry & Heidelbach, 2006; Angiboust et al., 2011; Keppler et al., 2016; Hertgen et al., 2017; Rogowitz & Huet, 2021). These heterogeneities are either due to heterogeneities in the protolith, chemical reactions, or deformation processes (e.g. Ji et al., 2003; Terry & Heidelbach, 2006; Hertgen et al. 2017).

The majority of eclogites have low to intermediate garnet content and develop an interconnected weak layer type of microstructure. Garnet-rich layers develop a load-bearing framework if the garnet fraction is approximating 75% (e.g. Rogowitz et al., 2023). The fabrics that develop in compositionally heterogeneous eclogites reflect the rheological contrast of their primary constituents. Omphacite-rich domains or layers exhibit mylonitic fabrics with networks of conjugated micro-shear zones, indicating strain localization of crystal-plastic character (e.g. Angiboust et al., 2011; Hertgen et al., 2017; Rogowitz et al., 2023). Analogous networks of brittle character also occur in garnet-rich domains or layers, revealing cataclastic fabrics (e.g. Angiboust et al., 2011; Hertgen et al., 2017; Rogowitz et al., 2023).

2.2.4. Deformation Mechanisms and Microstructures

The dominant operative deformation mechanisms in eclogites' major constituents vary greatly depending on their relative proportions, grain size, competence contrast, the P/T conditions of deformation, peak stress, strain rate, accumulated strain, and fluid content. While both garnet and omphacite require high stress in order to creep, garnet is generally 4 – 6 times stronger than omphacite (Zhang & Green, 2007). The high rheological contrast induces high stress concentrations (Kenkmann & Dresen, 1998), causing strain to localize at the interfaces between garnet and omphacite (e.g. Rogowitz et al., 2023). However, evidence from UHP/HT eclogites suggests that the rheological contrast between garnet and omphacite could be significantly reduced (e.g. Ji et al. 2003).

The development of garnet's SPO and omphacite's variation in CPOs have been the subject of numerous investigations over the past few decades. Several field-based and experimental microstructural investigations, as well as studies based on numerical simulations have proposed various small-scale mechanisms responsible for these textures. In an attempt to provide some clarity on this topic, the following is a literature review of notable constraints on the operative deformation mechanisms in omphacite and garnet, along with indicative microstructures.

2.2.4.1. Omphacite

Omphacite predominantly accommodates strain in eclogites, typically exhibiting extensive crystal-plastic deformation characterized by a pronounced CPO and SPO. Brittle deformation is usually expressed in the form of micro-faults originating from fractured garnet grains. It is induced either by seismic strain rates (e.g. Broadwell et al., 2019), the influence of fluids, strain localization due to mesoscopic lithological heterogeneities (e.g. Hertgen et al., 2017), or high garnet content (e.g. Rogowitz et al., 2023).

Several early studies have discussed omphacite's general weakness relative to garnet and have set its viscous creep field lower boundary at 500 – 600° C (e.g. Philippot & van Roermund, 1992). However, Stöckhert & Renner (1998) showed that omphacite's strength varies significantly according to its modal jadeite-diopside (Jd-Dio) composition, with higher jadeite fractions resulting in weaker omphacite. This observation is in accord with microstructural evidence for dislocation creep and recrystallization by subgrain rotation below 500° C (e.g. Lardeaux et al. 1986; Piepenbreier & Stöckhert, 2001).

At low temperatures but elevated strain rates, omphacite's crystal lattice distortion is usually transpiring through dislocation glide on an easy-slip system. Dislocation glide dominance is indicated by undulatory extinction and a pronounced L-type CPO, in the absence of SPO (e.g. Godard & van Roermund, 1995; Piepenbreier & Stöckhert, 2001). Dislocation glide is typically accompanied by dynamic recrystallization through bulging, which results in the formation of small, strain-free crystals with low misorientation angles.

Omphacite's typical SPO is characterized by elongated/flattened grains or crystals and is a result of either dissolution-precipitation at high-pressure and/or in fluid-rich environments, or high-temperature crystal-plastic mechanisms, such as dislocation creep and diffusion creep. Diffusion creep is grain-size sensitive, i.e. it dominates in fine-grained omphacite, and is indicated by chemical maps. Due to omphacite's significant anisotropy, diffusion rates are an order of magnitude higher in one crystallographic direction causing oriented crystal growth, typically leading to an S-type CPO (e.g. Mauler et al., 2001). Dissolution-precipitation is indicated by pressure-solution seams; concomitant diffusion and preferred pressure-solution of grains oriented perpendicular to the foliation enhances the S-type CPO (e.g. Rogowitz & Huet, 2021). At high temperatures and strain rates, omphacite's SPO develops due to dislocation creep, which is indicated by subgrains, orientation contrast, high dislocation densities, and a pronounced CPO, which can be L-type due to activation of an easy-slip system, or S-/SL-/LS-type due to activation of multiple slip-systems (e.g. Bascou et al, 2001; Zhang et al., 2006). Dislocation creep is typically accompanied by recovery and dynamic recrystallization through subgrain rotation or grain boundary migration. Recovery operates through dislocation climb, indicated by low-angle subgrain boundaries. Dynamic recrystallization is indicated by extensive grain-size reduction; subgrain rotation is promoted by elevated strain rates, and grain boundary migration is promoted by elevated temperatures or high misorientation angles. Extensive subgrain rotation leads to grain boundary migration (e.g. Piepenbreier & Stöckhert, 2001), although increases in strain rate may reverse this transition (e.g. Keppler et al., 2016).

Omphacite exhibits strong variations in CPO, corresponding to variations between L- and S-type fabrics, with pure S- and L- type fabrics being as common as SL- and LS- type fabrics. These variations are typically explained by the concurrent/sequential operation of diffusion and dislocation creep. However, the variations in CPO have also been explained by the operation of diffusion creep with concomitant dissolution-precipitation (e.g. Mauler et al., 2001), dynamic recrystallization by subgrain rotation and grain boundary migration (e.g. Keppler et al., 2016), or the exclusive operation of dislocation creep (Zhang & Green, 2007). Dislocation creep facilitates variations between L-type and S-type fabrics due to the simultaneous activation of multiple slip-systems through the rotation and shape variation of the finite strain ellipsoid (Zhang & Green, 2007).

Besides temperature, strain rate, and its modal Jd-Dio composition, garnet content in eclogites plays a crucial role in determining the operative intracrystalline deformation mechanism in omphacite, due to the stress concentrations induced by their significant rheological contrast. A moderate increase in garnet content induces a transition from distributed dislocation glide to localized dislocation creep accompanied by stress-induced grain size reduction through dynamic recrystallization (Rogowitz et al., 2023).

2.2.4.2. Garnet

Garnet typically exhibits rigidity with minor crystal-plastic deformation at temperatures below 750° C. Below 600°C, minor localized intracrystalline-plasticity features are common in garnet; these are usually limited to stress concentrated areas (e.g. Voegelé et al., 1998). The strain localization caused by the increased stress concentrations at fractures or rheological heterogeneities induces minor dislocation activity, which is usually manifested as increased misorientation, low-angle grain boundaries, and increased dislocation density. Although uncommon, there have been instances where dominant dislocation creep with dynamic recrystallization has been documented in garnets deformed even below 600° C (e.g. mylonites: Massey et al., 2011).

Garnet's brittle deformation is commonly expressed in the form of microfractures and micro-faults; it was previously attributed exclusively to seismic either strain rates (e.g. Angiboust et al., 2011; Broadwell et al., 2019), strain localization due to lithological heterogeneities, or the influence of fluids (e.g. Hertgen et al., 2017). However, several other factors could induce brittle failure in garnet, such as its mineral composition (Katayama & Karato, 2008), elevated but non-seismic strain rates, and locally higher stress fields at grain boundaries (Yamato et al., 2019). The latter is promoted by a higher garnet content in eclogites, particularly in compositions resembling LBF microstructures (Rogowitz et.al, 2023).

Despite its general rigidity, garnet develops an SPO, defined by elliptical/flattened/elongated clusters or grains. Elongated grains have been frequently attributed to oriented growth mechanisms during crystallization. Garnet flattening can transpire without internal deformation through rigid body rotation and grain boundary sliding, indicated by garnet tails consisting of heterogeneous grain size (Rogowitz et al., 2023). Cataclasis, usually operating at low temperatures and pressures but high strain rates, is also a viable deformation mechanism for SPO development in garnet (Trepmann & Stöckhert, 2002). It is indicated by a high fracture density, irregularly shaped fragments, and heterogeneous grain size reduction. At high temperatures, fine-grained garnet can be effectively flattened through diffusion creep, indicated by chemical mapping (e.g. Philipps & Ji, 2021). At elevated pressures and/or in fluid-rich environments, garnet's SPO typically develops through dissolution-precipitation creep; its dominance is indicated by the truncation of crystal growth zonations, and by pressure-solution surfaces parallel to the SPO, in the absence of crystal lattice distortion features (e.g. Philipps & Ji, 2021). Pressure-solution rates are faster in crystals with a higher dislocation density (e.g. Schott et al., 1989), which may result in grain coarsening, as smaller, distorted crystals are dissolved and reprecipitated onto larger grains (e.g. Rogowitz & Huet, 2021).

Regarding garnet's intracrystalline plasticity, the operation of processes such as dislocation creep and related dynamic recrystallization has been controversial for many years. Due to garnet typically exhibiting a weak or random CPO (e.g. Bascou et al., 2001; Zhang & Green, 2007; Massey et al., 2011; Philipps & Ji, 2021), very high creep strength in rheological experiments (e.g. Karato et al. 1995; Jin et al., 2001; Zhang & Green, 2007), low dislocation density compared to its coexisting minerals (e.g. van Roermund, 1983), and dislocations with long lengths of Burgers vectors (Allen et al., 1987), the operation of dislocation creep is not self-explanatory.

Garnet has a large number of slip-systems for dislocation movement and a high lattice friction, thus, in most cases, a random or weak CPO develops even if dislocation creep is dominant (Mainprice et al., 2004). A strong CPO develops only if very high temperatures and high strains are prevalent (e.g. Bergen arc garnets: Boundy et al., 1992). Moreover, due to garnet crystallizing in a cubic crystal system, its optical isotropy renders the examination of substructures with optical microscopy impossible; modern techniques such as orientation contrast or electron backscatter diffraction are thus required. By utilizing such techniques to measure the orientations of subgrains and low-angle grain boundaries, the operation of dislocation creep can be confirmed by verifying a rotational dispersion of these measurements around crystallographic axes. Hence, dislocation creep has been evidenced in several cases, including recrystallized porphyroclasts found in mylonites deformed under high strains, at temperatures as low as ~600° C (Massey et al., 2011) and ~700° C (Prior et al., 2002). Furthermore, high-temperature recovery-accommodated dislocation creep dominance has been evidenced in elongated mantle garnets (e.g. Prior et al., 2000).

Development of garnet's SPO may also transpire through dominance of grain boundary processes, as has been shown in a systematic experimental investigation by Zhang & Green (2007). They demonstrated that garnet's creep strength reduces significantly in wet conditions and under high shear strain. High strains cause omphacite to extensively flow, sweeping garnet into clustered bands. Under wet conditions, the banding of garnet occurs even at low strains. This clustering of garnet into layers leads to high stress concentrations at grain boundaries, resulting in local dislocation activity. Analyses from this study revealed that the flattened garnet clusters were not dominated by dislocation creep, but rather occurred through dynamic recrystallization driven by grain boundary processes: extensive grain boundary sliding enhanced by subgrain rotation. Grain size reduction in the proximity of grain boundaries and sliding of small grains into the foliation are indicative of deformation through grain boundary sliding.

Storey and Prior (2005) conceptualized a strain-dependent evolution model for garnet porphyroclasts: they first deform by recovery-accommodated dislocation creep, followed by subgrain rotation dynamic recrystallization, and finally diffusion-assisted grain boundary sliding. Grain boundary sliding is assisted by diffusion creep as the reduced grain size due to dynamic recrystallization favors diffusive mechanisms. It operates commonly alongside grain rotation ('rotation jump'), and dislocation creep, as crystals continue to deform internally; it is accommodated by recovery and sometimes grain boundary migration recrystallization (e.g. Bestmann et al., 2008). An analogous high temperature mechanism is dislocation-assisted diffusion creep, proposed by Phillips & Ji (2021) for the Morin garnets. The fine-grained Morin garnets were effectively deformed by volume diffusion creep with fast diffusion rates, whereas volume diffusion of larger grains was assisted by dislocation activity. Both the grain boundary sliding, and diffusion creep processes enhance the randomization of CPO (Bestmann et al. 2018; Mainprice et al., 2004).

In summary, dissolution-precipitation creep dominates under eclogite facies conditions (HP), dislocation-assisted diffusion creep dominates under granulite facies conditions (HT), and recovery-accommodated dislocation creep along with grain boundary processes (subgrain formation/rotation and grain boundary sliding) dominate the intermediate pressure-temperature space (Philipps & Ji, 2021).

2.2.5. Strain Weakening and Strain Localization

Transformation of dry mafic rocks into eclogites typically transpires in fluid-rich subduction zones; fluids facilitate transformation by either acting as catalysts or exerting thermodynamic influence (e.g. Putnis and Austrheim, 2010). Infiltration of fluids occurs through fracture networks and/or microporosity that develops due to volume decrease during eclogitization (e.g. Engvik et al., 2007); this process functions as a positive feedback loop, as the volume decrease induces further fracturing and thus also strain weakening. Moreover, fracture networks act as brittle precursors for localized shear zones of ductile character (e.g. Menegon et al., 2017), resulting in further fluid infiltration (e.g. Fusseis et al., 2009) and strain weakening. Apart from eclogitization, fluids facilitate hydrolytic weakening and metamorphic reaction-induced weakening (e.g. Griggs, 1967; Engvik et al., 2007). Furthermore, eclogitization assisted by dissolution-precipitation induces rapid phase-transformational and volumetric mechanical strain weakening (Rogowitz & Huet (2021). All of this contradicts the general assumption that eclogites are highly resistant to deformation, as the processes which produce eclogites could also potentially weaken them.

The rheological weakening and strain localization of eclogites are typically associated with lithospheric processes at convergent plate boundaries (e.g. Jolivet et al., 2005; Angiboust et al., 2011). Although subduction zones are predominantly influenced by fluids (e.g. Wassmann & Stöckhert, 2013), numerous convergent settings are dehydrated post-eclogitization (e.g. Engvik et al., 2007). However, strain localization has been documented in mylonitic eclogites and interpreted to have occurred post-eclogitization, suggesting that weakening by eclogitization and fluid-related processes may not be viable mechanisms (e.g. Engvik et al., 2007). Brittle precursors associated with seismic strain rates often result in strain localization and weakening in dry conditions (e.g. Austrheim et al., 2017). Conversely, numerical simulations by Yamato et al. (2019) showed that increasing garnet content could potentially introduce brittle precursors in dry eclogites deforming at non-seismic strain rates. Furthermore, a recent experimental investigation coupled with numerical simulations by Rogowitz et al. (2023), showed that garnet content is a crucial factor in the occurrence and intensity of strain localization and strain weakening in dry conditions. The study underlined the mechanisms of strain weakening and localization of dry eclogites. Pure omphacite and 25% garnet samples (IWL) examined in this study exhibit minor strain weakening, attributed to distributed dislocation glide and CPO development within the omphacite matrix. The rheological contrast between garnet and omphacite induces stress concentrations in the matrix (e.g. Handy, 1990; Kenkmann & Dresen, 1998). As a result, increased garnet content enhances crystal-plasticity in omphacite, promoting the onset of strain localization at the yield point and thus intensifying strain weakening. In samples with 50% garnet (IWL), brittle precursors originating in garnet lead to the nucleation of recrystallized, conjugated micro-shear zones within omphacite-rich domains. Samples with 75% garnet (LBF) also exhibit intense strain weakening, attributed to brittle conjugated micro-shear zones nucleated at garnet neck domains. These garnet neck domains concentrate stress, inducing localized strain hardening, which leads to brittle failure. The observed grain size reduction, in both recrystallized and brittle micro-shear zones, facilitates the accommodation of localized strain (De Bresser et al., 2001), resulting in a more intense strain weakening response.

3. MATERIALS AND METHODS

3.1. Experimental Methods

A total of four dry eclogite samples were synthesized with a composition of 75% omphacite volume fraction – 25% garnet volume fraction. One sample (PE01) was kept undeformed for reference, and the remaining three were axially shortened using a high pressure/high temperature Griggs-type deformation apparatus. Two samples (PE02, PE04) were deformed slightly, close to the material's yield point, and one sample (PE03) was deformed up to a high degree of strain. The implemented conditions of deformation were 2.5 GPa confining pressure, 900° C confining temperature, and $6.4 \cdot 10^{-6}$ s^{-1} strain rate.

3.1.1. Starting Material and Synthesis

The source of the starting material is natural eclogite from the type locality Hohl in the Koralpe (Miller & Thoni, 1997). The starting material was prepared by Katrin Kraus. Crushing and grinding the source material resulted in mixed mineral powders. Garnet was separated from omphacite based on their gravimetric and magnetic properties. The separated minerals were ground again and sieved down to a grain size of 40 – 70 μm, which is ideal for promoting dislocation creep processes.

A total of four dry eclogite samples were synthesized by Sarah Incel. The starting material was mixed and sealed inside thin, cylindrically shaped gold jackets to form omphacite-rich crystal mixtures (75% vol. omphacite – 25% vol. garnet). The mixtures contained a few impurities (totaling at less than ~5% volume; they should not influence the rheology), such as titanite, rutile, amphiboles and clinozoisite. Synthesis was carried out inside a hydraulic piston cylinder press, using a sodium chloride confining medium. The mixtures were first cold pressed at 3 MPa, before hot pressing them at 3 GPa and 1100° C for 24 hours.

3.1.2. Deformation Experiments

Three out of the four synthesized samples were axially compressed in a servohydraulically-controlled, modified Griggs-type deformation apparatus (Griggs, 1967; Rybacki et al., 1998); the structure of the apparatus is schematically shown in Figure 5. The applied deformation conditions were 2.5 GPa confining pressure, 900° C temperature, and $6.4 \cdot 10^{-6}$ s^{-1} strain rate.

Pressure build-up is achieved by advancing the confining piston into the pressure vessel. To ensure isotropic force distribution, a solid salt (NaCl) confining medium was used. The Griggs apparatus contains a deformation piston, which moves independently from the confining piston, and is responsible for creating an anisotropic stress field by introducing a uniaxial compressive stress component. Heating is accomplished by an electrical connection with a graphite resistance furnace, which is part of the sample assembly. The axial displacement of the two pistons is controlled and digitally recorded by two external linear variable displacement transducers (LVDT, ~0.2% accuracy). The oil pressure is measured by a high precision gauge (~0.2% accuracy), and two thermocouples control and record the temperature inside the vessel (accuracy: ± 20° C). An external load cell measures the axial load with an accuracy of ~0.02% (Rybacki et al., 1998).

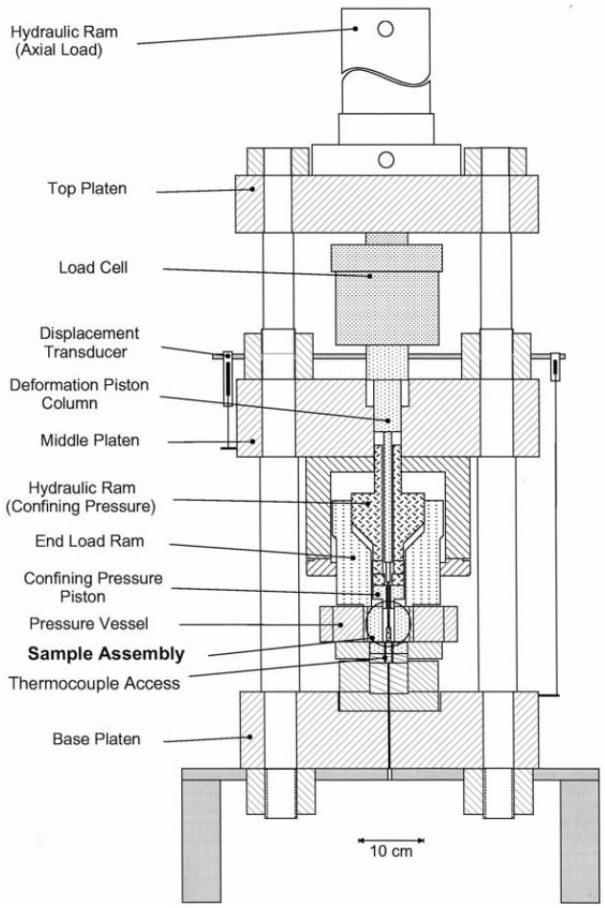

Figure 5: Anatomy of the Griggs deformation apparatus. It consists of a fixed top, middle and base plate. The deformation column includes two hydraulic rams, an external load cell, a deformation piston, and a confining piston. The sample assembly is located inside a pressure vessel (Rybacki et al., 1998).

All deformation experiments were conducted using a solid salt sample assembly, slightly modified from the original by Rybacki et al. (1998). The sample assembly consists of a set of concentric rings, tubes, and cylinders used mainly for sealing and minimizing friction; its structure is shown in Figure 6. The gold jacket containing the sample is located at the core of the sample assembly on a ceramic pedestal, enclosed by an inner salt tube. Details on the construction and the different parts of the sample assembly are available in Appendix a.

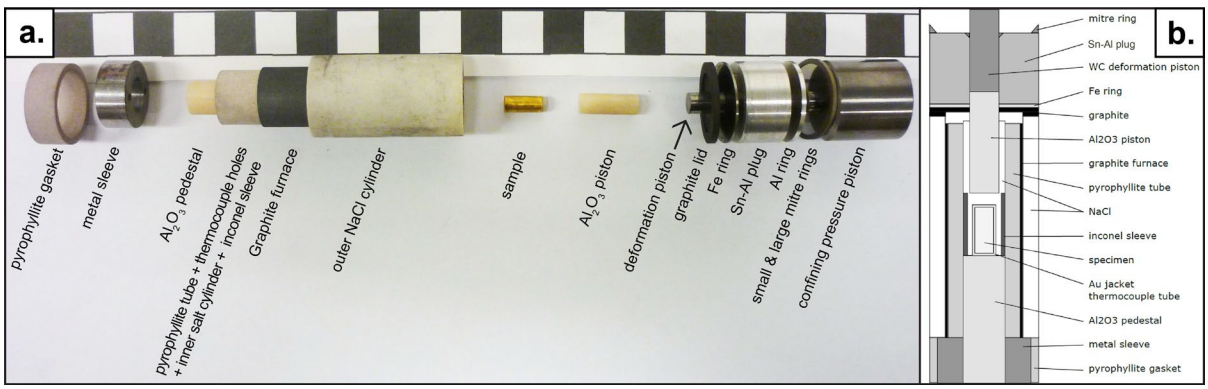

Figure 6: (a) Photograph of all the parts constituting the solid-salt sample assembly (Incel, 2017). (b) Sketch of the solid salt sample assembly (Rybacki et al., 1998, figure modified by Kraus, K.).

3.1.2.1. Experimental Procedure

Three out of the four synthesized samples were mechanically sealed into new gold jackets, and the sample assembly was constructed. The base plate and pressure vessel, including the sample assembly, were inserted into the Griggs deformation apparatus, and the heating and cooling systems were connected. A detailed protocol of the experimental procedure and a summary table of experimental details are available in Appendix a. Deformation experiments lasted approximately 43 hours and include three phases:

- Heating/pressurizing phase: To ensure a confining pressure build-up of hydrostatic nature, slow heating/pressurizing ramps were implemented. For pressure build-up, the W50 LVDT (50 mm range) was used to advance the confining piston until reaching the target oil pressure of 78.62 MPa, which corresponds to 2.5 GPa confining pressure (conversion factor: 31.8). The heating ramps were controlled by a power supply connected to the thermocouples. During the early heating/pressurizing phase (until ~500° C), the recorded load was constantly monitored, and the W50 LVDT's position was adjusted accordingly to prevent separation incidents that occurred in the deformation column due to frictional forces.
- Deformation phase: The W5 LVDT (5 mm range) was used to advance the deformation piston with a constant velocity of 0.185 mm/h (0.182 mm/h for the shorter sample PE03). This corresponds to a constant strain rate of $6.4 \cdot 10^{-6}$ s^{-1}, computed by the formula $V = SR * LS$ (V = velocity, SR = strain rate, L_S = sample length). During the early deformation phase, the hit point was identified by a change in curvature of the recorded load-time curve in order to calculate the remaining deformation time.
- Cooling/depressurizing phase: The deformation piston was retracted before applying a slow cooling and depressurizing ramp. Slow depressurizing prevents the occurrence of decompression cracks in the sample. Samples were extracted from the pressure vessel using a hydraulic press.

3.1.2.2. Mechanical Data

True axial differential stress and true axial strain values were derived from the recorded load and displacement values respectively, by correcting the data for the internal stiffness and friction of the apparatus. System stiffness and friction corrections were carried out by implementing a Matlab® script (https://www.mathworks.com/products/matlab.html), by assuming constant sample volume. The script is broken down in Appendix b. The uncertainty in true axial differential stress values is estimated at ± 0.2 GPa, considering the uncertainties in the accuracy of the external load cell, sample diameter measurement, and the uncertainty in friction correction (Druiventak et al., 2011). The uncertainty in true axial strain values is estimated at 0.1%, considering the uncertainties in the accuracy of the LVDT, and the uncertainty in stiffness correction (Moghadam et al., 2010). Measured confining pressure is also affected by the internal friction and stiffness, and it can deviate up to 10% from the actual confining pressure (Moghadam et al., 2010). Strain rate uncertainty (~10%) in the reported values arises from the uncertainty of sample length measurement (Moghadam et al., 2010).

3.2. Microfabric Analysis

The microfabrics of the experimental samples were examined by performing a series of microstructural analyses both in two dimensions (2D) and in three dimensions (3D). The 2D analyses included optical microscopy and scanning electron microscope (SEM) imaging. SEM imaging provided qualitative composition (z-contrast) and qualitative crystallographic orientation contrast (OC) data. The microstructures observed in the 2D data were interpreted to identify the dominant deformation mechanisms in each of the experimental samples. The 3D analyses were performed using an x-ray microtomography instrument (micro CT) to quantitatively measure the volume, 3D shape, and spatial arrangement of garnet and omphacite. The 3D data were processed with the Avizo® software (http://www.fei.com/software/avizo3d/) to quantify the volume of the two primary phases and the 3D interconnectivity of garnet clusters at varying strain levels. Additionally, the fabric tensor was calculated to quantify the degree of shape anisotropy and the elongation index of garnet and omphacite. The star length distribution (SLD) and star volume distribution (SVD) methods, included in the Quant3D software (Ketcham & Ryan, 2004), were employed for the fabric tensor calculations.

3.2.1. Optical and Scanning Electron Microscopy

Two-dimensional microfabric analysis was carried out using an optical microscope and a FEI Quanta 3D FEG scanning electron microscope (SEM). The SEM was utilized to acquire z-contrast and orientation contrast (OC) images. Thin sections with a thickness of 30 μm were prepared by Ilka Wünsche by cutting the experimental samples along their long axis and mechanically polishing them. For the OC analysis, the thin sections underwent chemo-mechanical polishing for approximately 3 hours, followed by carbon coating. The settings implemented for the SEM operation include an accelerating voltage of 15 kV, a working distance of 9.8 – 13.6 mm, a beam current of 4 nA set to analytical mode, a spot size of 1, and for the OC analysis, a sample tilt of 70°. The backscatter electron (BSE) detector was employed for z-contrast imaging, the forward scatter detector (FSD) for the OC analysis, and the x-ray detector for energy dispersive x-ray (EDX) analysis.

3.2.2. X-Ray Microtomography

A three-dimensional data collection was performed utilizing an x-ray microtomography instrument (micro CT). The scanning process was executed by Ian Butler, by employing high energy beam settings to maximize the contrast between the two primary phases, which was anticipated to be minimal due to the presence of high-density impurities (and residue gold particles from the gold jackets). The downside of utilizing high energy beam settings is the occurrence of an artifact known as the beam hardening effect, which manifests as concentric, circular bands with alternating brightness intensity. As the experimental samples exhibit variable heights, each sample required a distinct number of scans to sweep through its entire volume; larger samples demanded multiple scans. Table 1 displays the physical height of each sample, and the number of scans and cubic voxel side length of each microtomographic data set.

Table 1: Sample height, number of scans, and voxel size.

Sample №	Height (mm)	No. of scans	Cubic voxel side length (μm)
PE01	2.50	1	3.363
PE02	7.38	4	3.153
PE03	3.89	2	3.643
PE04	7.05	4	3.153

The Octopus Reconstruction® software, based on the filtered back-projection algorithm (Dierick, et al. 2004), was employed to obtain volumes of microtomographic slices from the projections. Reconstruction was meticulously conducted by Ian Butler to mitigate the beam hardening effect.

To facilitate the subsequent segmentation process, the reconstructed microtomographic slice stacks were batch-processed with a denoising filter. Specifically, the 2D Anisotropic Diffusion Filter plug-in (Tschumperle & Deriche, 2005), included in the Fiji® software (Schindelin et al., 2012), was implemented. This filter reduces random brightness heterogeneities present in the microtomographic slices due to noise, while retaining coherent edges. The filtering settings used are listed in Appendix c.

Following the filter application, the partial microtomographic slice stacks were aligned using residue gold particles as markers and were merged into a single stack for each sample. The 'reslice' function in Fiji® was applied subsequently to acquire stacks of vertical slices. By scrolling through a sample's volume vertically, domains with increased deformation were identified and the corresponding slices were extracted for image segmentation. Figure 7 presents four examples of denoised microtomographic slices, extracted from the core of the volume of interest (VOI) of each sample.

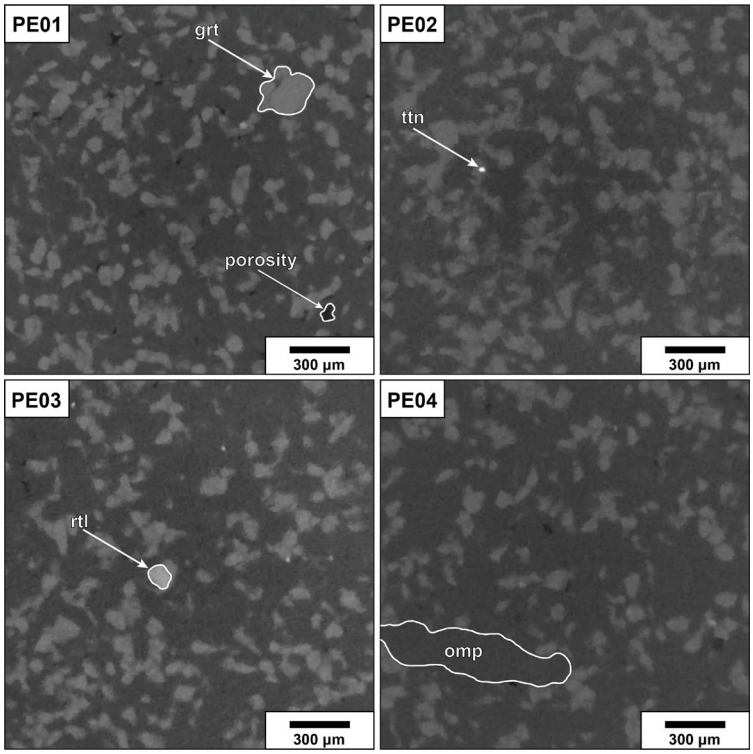

Figure 7: Denoised microtomographic slices from the core of the volume of interest of samples. The low contrast between the two primary phases is apparent; both are depicted in intermediate shades of gray. Garnet clusters (grt) are denser than omphacite (omp), thus they emit a more intense signal, depicted in slightly higher brightness values. A few of the contained irrelevant phases are marked, illustrating that the samples' components' signal responses cover the entire grayscale spectrum. Areas depicted in almost completely black colors are empty voids, part of the samples' microporosities. The mineral phase rutile (rtl) is depicted in slightly brighter shades of gray than garnet, and a tiny area, occupied by titanite (ttn), is depicted in white color.

Segmentation was carried out with the Trainable Weka Segmentation 3D plug-in (Arganda et al., 2017) included in the Fiji® software. This plug-in comprises a collection of machine learning algorithms, embedded with a set of image features, enabling the generation of image segmentations based on voxel classification. The image feature operations employed to 'train' the classifier are listed in Appendix c. Despite using high energy beam settings, the contrast between garnet and omphacite was relatively low. This led to the partial volume effect (where voxels in the proximity of phase boundaries acquire integral values), which, in combination with the beam hardening effect, rendered the classifier 'training' process challenging. Nevertheless, the accuracy of segmentation was evaluated by calculating the volume fraction of each class using the label analysis operator in Avizo® software (see Subsection 3.2.2.1). The segmentation results are stacks of probability maps, that assign a probability value of belonging to either the omphacite or garnet class to each voxel (impurities and microporosity were excluded from segmentation).

3.2.2.1. Quantitative Volume and 3D Interconnectivity Analysis

Quantitative volume and 3D garnet interconnectivity analyses were performed by modeling subvolumes of the experimental samples using the Avizo® software. The segmented data were imported as stacks of 500 square-shaped slices (each containing 500×500 pixels), modeling cubic subvolumes with dimensions of 500^3 voxels (~ 4 – 6 mm^3). The thresholding values assigned for both omphacite, and garnet were 95%, such that only voxels with a minimum of 95% probability of belonging to either class were labeled. The volumes of impurities (~5% vol.) were not labeled.

The label analysis operator was implemented to calculate the volume fraction of voxels belonging to either the garnet or omphacite classes. It is noted that label analysis groups face-connected voxels of the same class into distinct objects, which do not correspond to individual grains or crystals, but rather represent volumes occupied by the class. Since omphacite is completely interconnected, its total volume corresponds to a single object. For garnet, it is assumed that labeled objects represent garnet grain clusters. Objects consisting of fewer than 125 cubic voxels (5×5×5 voxels, ~4000 – 6000 μm^3) were removed to minimize numerical errors caused by segmentation (Fusseis et al, 2012; Macente et al., 2017).

To quantify the interconnectivity of garnet clusters, the results of label analysis were utilized. In each of the models, a single object occupies most of the total garnet volume and is considered an interconnected garnet cluster. The remaining volume is represented by a list of objects with significantly lower volumes, which are considered isolated garnet clusters. To assess the volumes of isolated garnet clusters, the border kill operation was used; this operation filters-out objects that are connected to the margins of the model, as these could potentially be linked to garnet clusters existing outside the model. To further evaluate garnet's interconnectivity, the garnet objects were submitted to a single numerical erosion step. Erosion is a morphological operation which removes voxels not entirely surrounded by the same class; it evaluates the strength of cluster connections by breaking the weakest links between them. The interconnectivity of garnet clusters and the volumes of isolated garnet clusters were calculated using both the segmented and the 'eroded' data. The settings applied for the border kill and erosion operations are listed in Appendix c.

3.2.2.2. Quantitative 3D Shape Analysis

Microfabric analysis in 3D was expanded by evaluating the degree of shape anisotropy and the elongation index of garnet clusters and the omphacite matrix in all four experimental samples, using the 'eroded' segmented data to avoid numerical errors introduced by segmentation and to accentuate the shapes (e.g. Macente et al., 2017). The Quant3D software was utilized to calculate the fabric tensor via the star length distribution (SLD) and star volume distribution (SVD) methods. Calculation of the fabric tensor is based on a voxel-traversing directed secant algorithm (Ketcham & Ryan, 2004). The SVD method works by projecting lines from various random points within the interior of the analyzed phase into random directions until encountering a phase boundary; in the SVD method the lines are substituted by cones. Because the SVD uses cubed lengths, the differences between long and short lines are accentuated. The Quant3D software uses both the SVD and SLD methods to compute the eigenvalues (τ_1, τ_2, τ_3) and the eigenvectors (u_1, u_2, u_3) of the fabric tensor, the components of the fabric tensor itself, the degree of anisotropy (DA = τ_1/τ_3), the isotropy index (I = τ_3/τ_1), the elongation index (E = 1 - τ_2/τ_1) and the dimensional normalization factor (sum (τ)). The first eigenvalue (τ_1) is the magnitude of the primary eigenvector (u_1), which corresponds to the strongest fabric orientation. Additionally, the program outputs visualizations of the SVD and SLD results, illustrated as surfaces representing 3D rose diagrams. The surfaces are drawn by extending each point by the relative magnitude of each measurement along its corresponding orientation and interpolating all the endpoints. The settings applied to calculate the fabric tensors are listed in Appendix c.

4. RESULTS

4.1. Mechanical Data

The corrected stress-strain curves derived from axial compression experiments are shown in Figure 8. Deformation of samples PE02 (red curve) and PE04 (blue curve) is compared to sample D4 (orange curve), which is part of a series of experiments conducted by Katrin Kraus (unpublished). Comparison is reasonable, since the intrinsic and extrinsic conditions of deformation were identical for all samples. Deformation of sample PE03 was not possible to quantify because of complications during the experiment.

The stress-strain curve of sample D4 reveals the complete evolution of differential stress ($\Delta\sigma$), which is equivalent to the compressive strength of the material, with increasing strain (ϵ). For the implemented intrinsic and extrinsic conditions, the yield point is reached at ~5% axial strain, maximum compressive strength ($\Delta\sigma_{max}$) is reached at ~7% axial strain, and the material then enters a state of rheological weakening. Sample PE04 was deformed slightly, approximating the yield point after accumulating ~4.7% axial strain. Sample PE02 was deformed moderately, up to the point of maximum compressive strength, accumulating ~7% axial strain. Sample D4 was strain weakened, accumulating ~19.8% axial strain. Sample PE03 was deformed highly; although its stress-strain curve was not acquired, its axial shortening was physically measured at 42%. Table 2 summarizes the available mechanical data.

Table 2: Mechanical data from axial compression experiments at 2.5 GPa pressure, 900° C temperature, and $6.4 \cdot 10^{-6}$ s^{-1} strain rate. * The axial shortening of sample PE03 was physically measured.

Sample №	$\Delta\sigma_{max}$ (GPa)	$\Delta\sigma$ at ϵ_{max} (GPa)	ϵ at $\Delta\sigma_{max}$	ϵ_{max}
PE04	0.27	0.27	4.7%	4.7%
PE02	0.42	0.42	7.0%	7.0%
D4	0.42	0.23	7.6%	19.8%
PE03	–	–	–	42.0%*

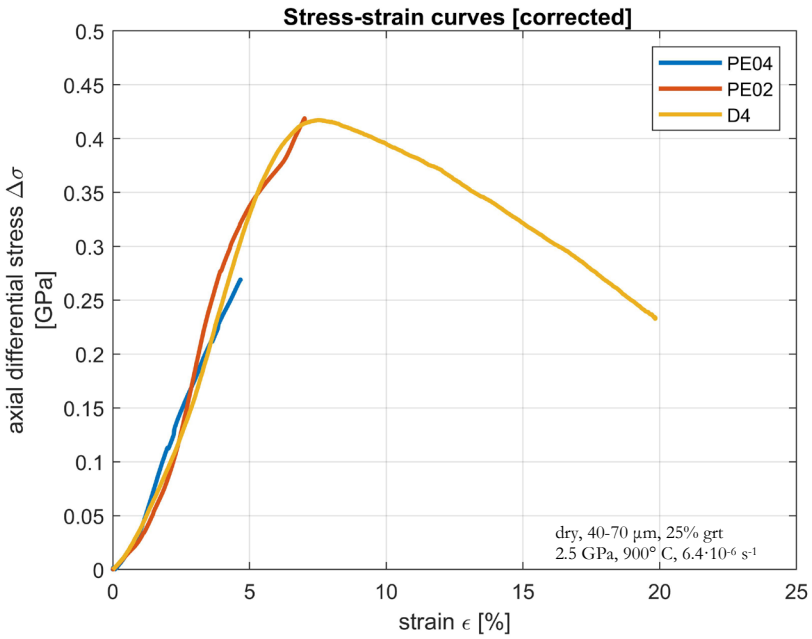

Figure 8: Stress-strain curves corrected for stiffness and friction. The experimental conditions are listed inside the plot.

4.2. 2D Microfabric Analysis

4.2.1. Overview

Overview BSE mosaics of all four experimental samples are ordered by increasing strain in Figure 9. All samples exhibit a matrix-supported microstructure, with garnet grains or clusters being surrounded by the omphacite matrix. The slightly and moderately deformed samples (PE04, PE02) appear similar to the undeformed sample (PE01), with isometric garnet grains, minor clustering, and no foliation. The highly strained sample PE03 reveals a reduced average grain size of garnet and a pronounced foliation, defined by sub-horizontal layering of flattened garnet clusters and elongated omphacite-rich domains.

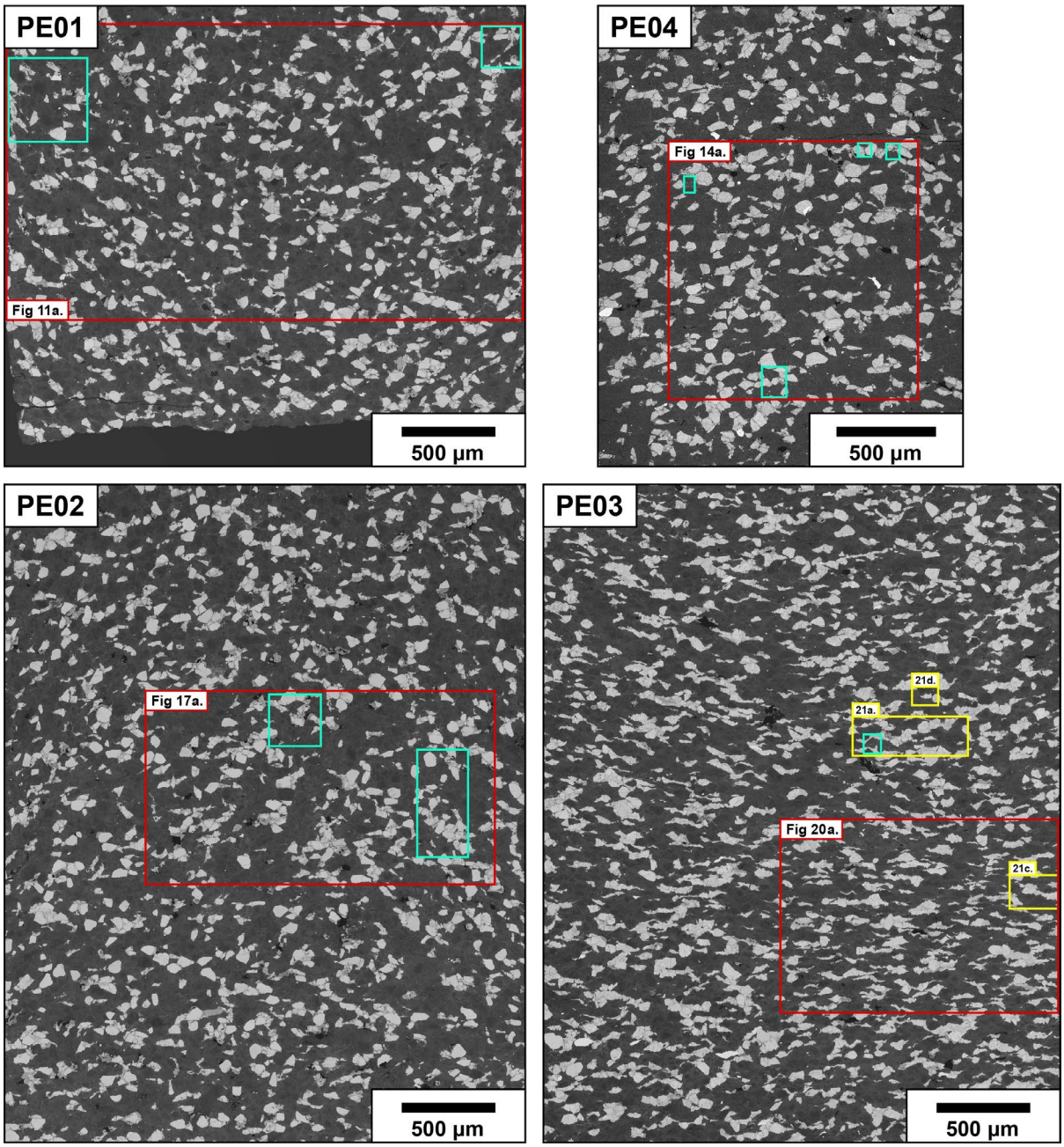

Figure 9: Overview BSE image mosaics of all samples arranged by increasing strain. The red and yellow rectangles mark BSE close-ups, yellow rectangles mark high resolution mosaics. The cyan rectangles mark localities of OC images.

4.2.2. PE01 (Undeformed)

Microfabric analysis of the undeformed sample reveals isometric garnet grains and randomly oriented garnet clusters within the omphacite matrix (Figure 9: PE01, Figure 10a, Figure 11a). Horizontal transgranular and intergranular cracks observed throughout the sample are interpreted as decompression cracks. Some microporosity is evident within the omphacite matrix, often situated at garnet-omphacite interfaces. Garnet clusters are composed of a few large grains (40 – 70 µm) surrounded by small, irregularly-sized fragments, which can be smaller than 10 µm (Figure 11b). Omphacite also exhibits a heterogeneous grain size, with large (50 – 100 µm), medium (10 – 50 µm), and small (< 10 µm) grains (Figure 10, Figure 12d).

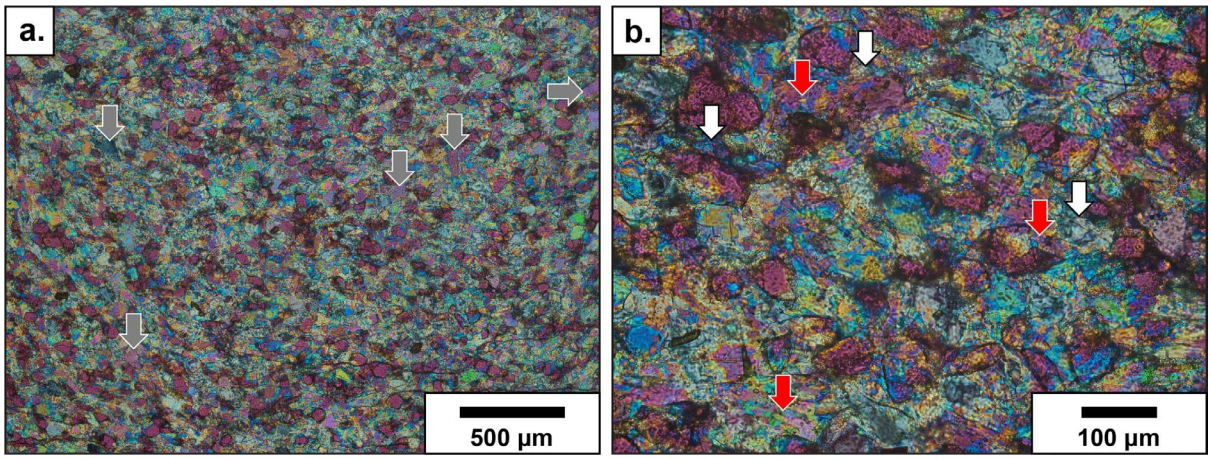

Figure 10: Optical photomicrographs of the undeformed sample (PE01). Crossed polarizers and lambda plate inserted. Gray arrows point to large, undeformed omphacite grains, white arrows point to undulatory extinction, and red arrows point to subgrains.

Analysis of omphacite under the optical microscope shows large undistorted omphacite grains (Figure 10a), and large internally deformed grains with undulatory extinction or subgrains. Distorted grains are usually situated within narrow domains squeezed in between garnet clusters (Figure 10b). Both observations are supported by OC analysis of omphacite, which reveals undistorted euhedral crystals (Figure 12d) and distorted omphacite grains with irregular grain boundaries and substructures, such as irregular internal OC or subgrains (Figure 12c-d).

Isolated garnet grains have straight to rounded grain boundaries and are often intact or sometimes slightly fractured by decompression cracks and their associated branches, and rarely by horizontal intragranular cracks (Figure 11a-b). Conversely, garnet grains within clusters are more frequently fractured and exhibit an increased fracture density towards grain boundaries, particularly near garnet-garnet contacts where the material is often fragmented in small fragments (Figure 11b). Grain boundaries of intra-cluster garnets are often angular or irregular and originate from fractures (Figure 11c). Intracrystalline deformation of garnet is minor, as OC images reveal no significant substructures. Larger grains have a slight, gradual internal OC towards domains with high fracture density, and a stronger OC appears between fragments within highly fractured domains (Figure 12d).

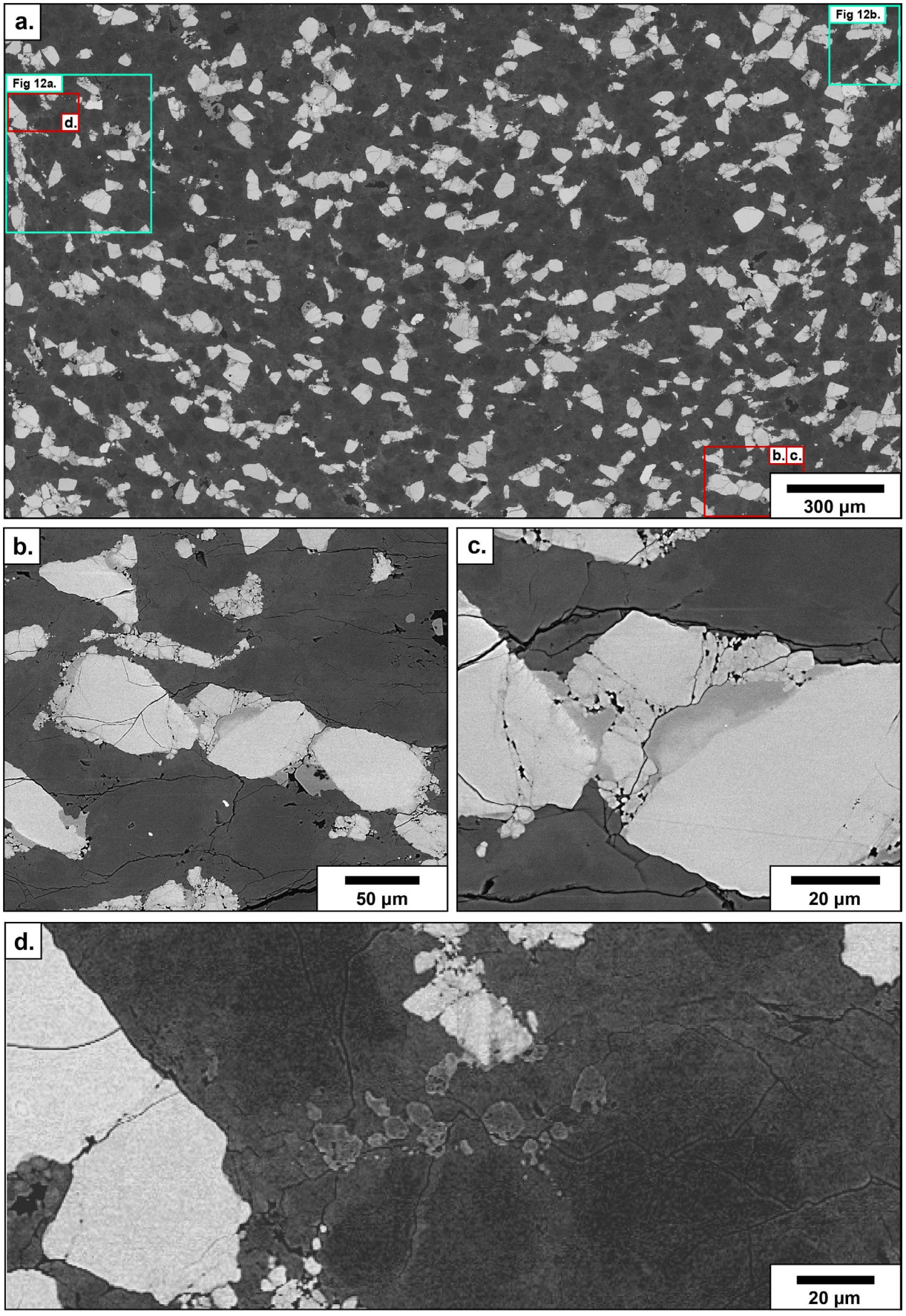

Figure 11: BSE images of the undeformed sample (PE01). The red rectangle marks the localities of close-ups, the cyan rectangles mark the localities of OC images. (a) Overview. (b) Garnet cluster with fractured contacts, zoning, and euhedral Mg-rich crystals. (c) Close-up of garnet-garnet contacts in (b). (d) Irregularly shaped, Mg-rich garnet crystals along fracture within omphacite.

Both garnet and omphacite grains exhibit a chemical zoning in the BSE images, which has been qualitatively assessed with EDX analysis. Omphacite grain rims appear in lighter gray shades and are enriched in Fe and depleted in Mg. Conversely, garnet grain rims appear darker and are enriched in Mg and depleted in Fe, particularly in the vicinity of garnet-garnet contacts (Figure 11b-c, Figure 12a-b). Similar chemical patterns occur along fractures in garnet. Moreover, the Mg-enriched garnet rims appear to extend into the microporosity, forming randomly-oriented, euhedral garnet crystals. EDX analysis of the euhedral garnet crystals revealed a composition similar to the garnet grain rims. Another observed feature are irregularly shaped, dark-shaded garnet crystals, which extend from the garnet rims along cracks within the omphacite matrix (Figure 11d). The irregular garnet crystals have a very thin rim with a similar Mg-enrichment as the euhedral crystals, but their main body is even more enriched in Mg.

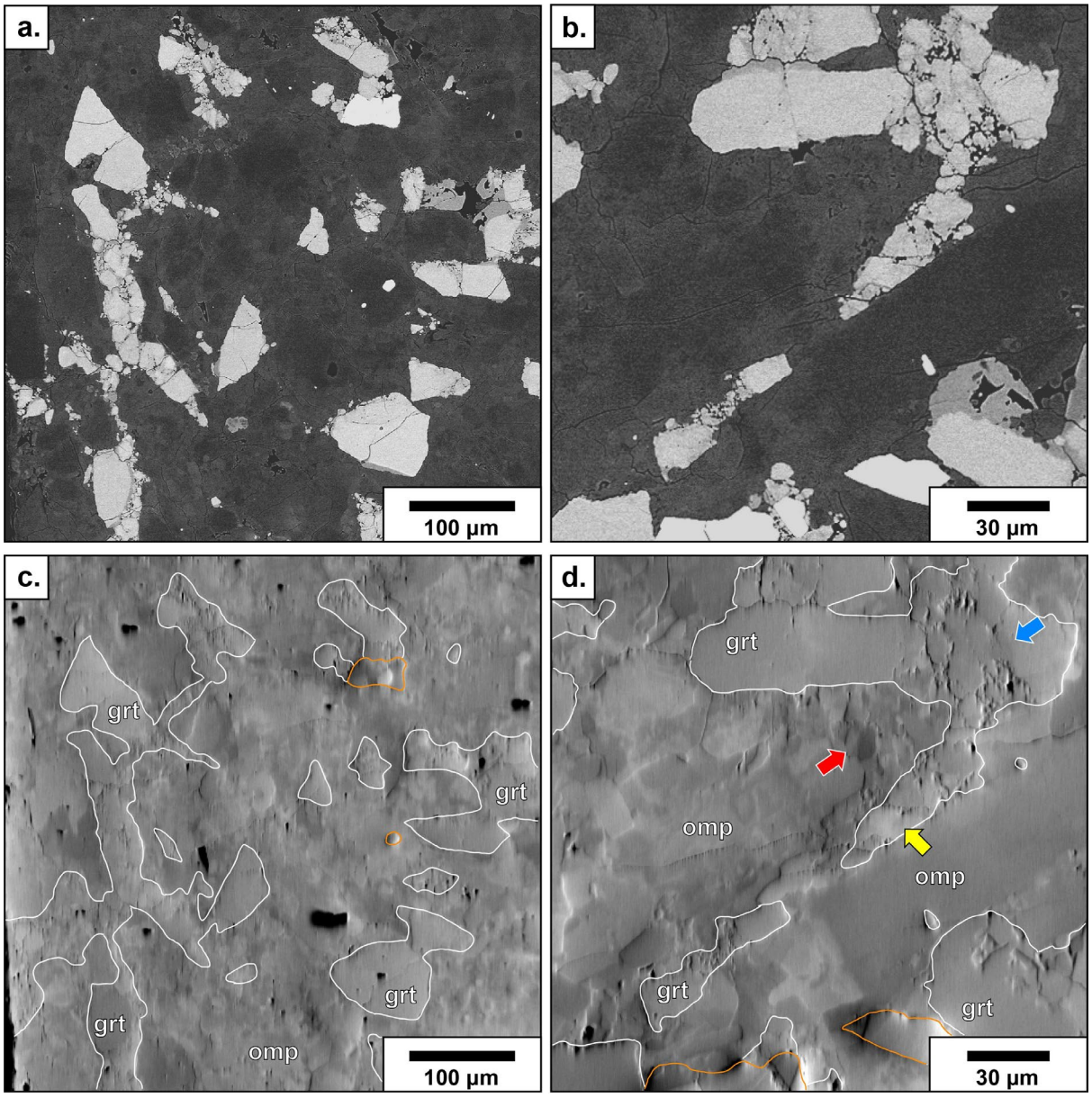

Figure 12: (a) and (b) BSE images of the undeformed sample (PE01). (c) and (d) Corresponding OC images. White borders mark interfaces between garnet and omphacite; orange borders mark grain boundaries of impurities. The yellow arrow points to OC between garnet's fragments, the blue arrow points to garnet's internal OC, and the red arrow points to omphacite subgrains.

4.2.3. PE04 (Yield Point – 4.7% Axial Strain)

The microfabric of the slightly deformed sample PE04 consists of isolated isometric garnet grains and clusters which are mostly randomly oriented within the omphacite matrix (Figure 9: PE04, Figure 13, Figure 14a). The sample features horizontal decompression cracks, microporosity, and chemical zonations of both garnet and omphacite; Mg-enriched euhedral (Figure 14d) and irregular garnet crystals are also observed (Figure 14f). Omphacite grain size ranges from a few micrometers to ~100 µm (Figure 13, Figure 15b-d). Garnet clusters are composed of a few large grains (40 – 70 µm) surrounded by irregularly-sized garnet fragments, which can be as small as a few micrometers (Figure 14b). Clusters are sometimes arranged sub-horizontally (Figure 14c, 14g), and the fragmented garnet material occasionally forms fine-grained tails perpendicular to the shortening direction (Figure 14f). However, randomly oriented garnet clusters are more abundant, thus no persistent SPO is evident in the sample (Figure 9: PE04, Figure 14a).

Omphacite exhibits minor brittle deformation in BSE images, usually linked to fractures originating from garnet clusters (Figure 14g) or associated with decompression cracks. A weak SPO, defined by large omphacite crystals (> 50 µm) that are elongated perpendicular to the shortening direction (Figure 13), is observed under the optical microscope. These elongated crystals are usually situated within narrow domains squeezed in between garnet clusters and exhibit undulatory extinction and occasionally subgrains or deformation twins. OC imaging reveals grain boundaries that are usually straight, and substructures, such as deformation twins, internal irregular OC, and subgrains (Figure 15b-d). The fractured domains displayed in Figures 15b and 15d exhibit a higher concentration of small grains and subgrains.

BSE analysis of garnet reveals that isolated grains are often undisturbed and have straight to rounded grain boundaries, whereas garnet clusters exhibit fracture-dense domains. Grain boundaries within clusters are angular or irregular, and often originate from fractures (Figure 14g). Vertical and randomly oriented intragranular cracks in intra-cluster garnets are common, and they sometimes extend into the omphacite matrix (Figure 14d, 14g). An OC between garnet fragments, and minor substructures, such as subgrains and gradual internal OC towards fractures are visible in OC images (Figure 15a-b, 15d).

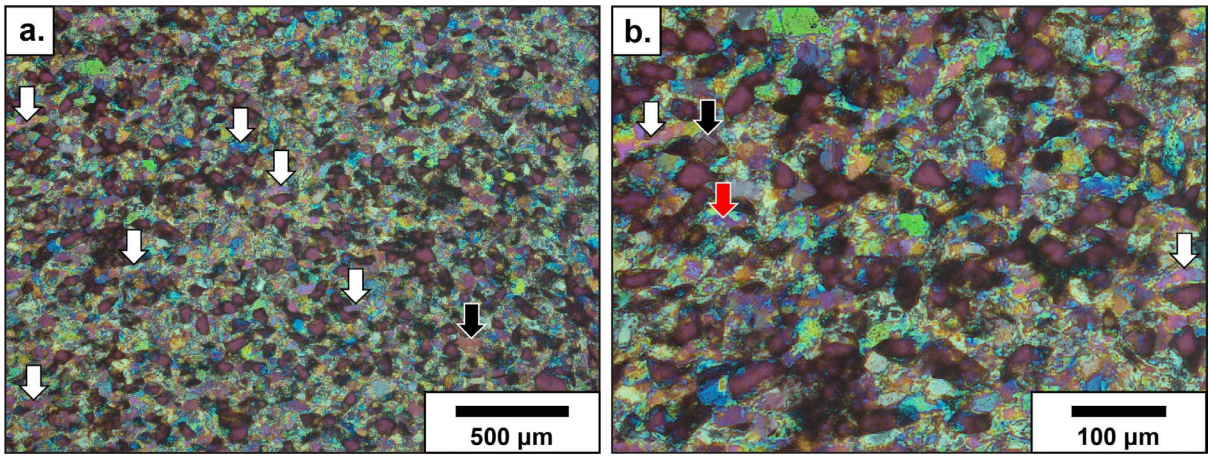

Figure 13: Optical photomicrographs of the slightly deformed sample (PE04). Crossed polarizers and lambda plate inserted. White arrows point to elongated omphacite grains with undulatory extinction, black arrows point to twinned omphacite grains, red arrow points to omphacite subgrains.

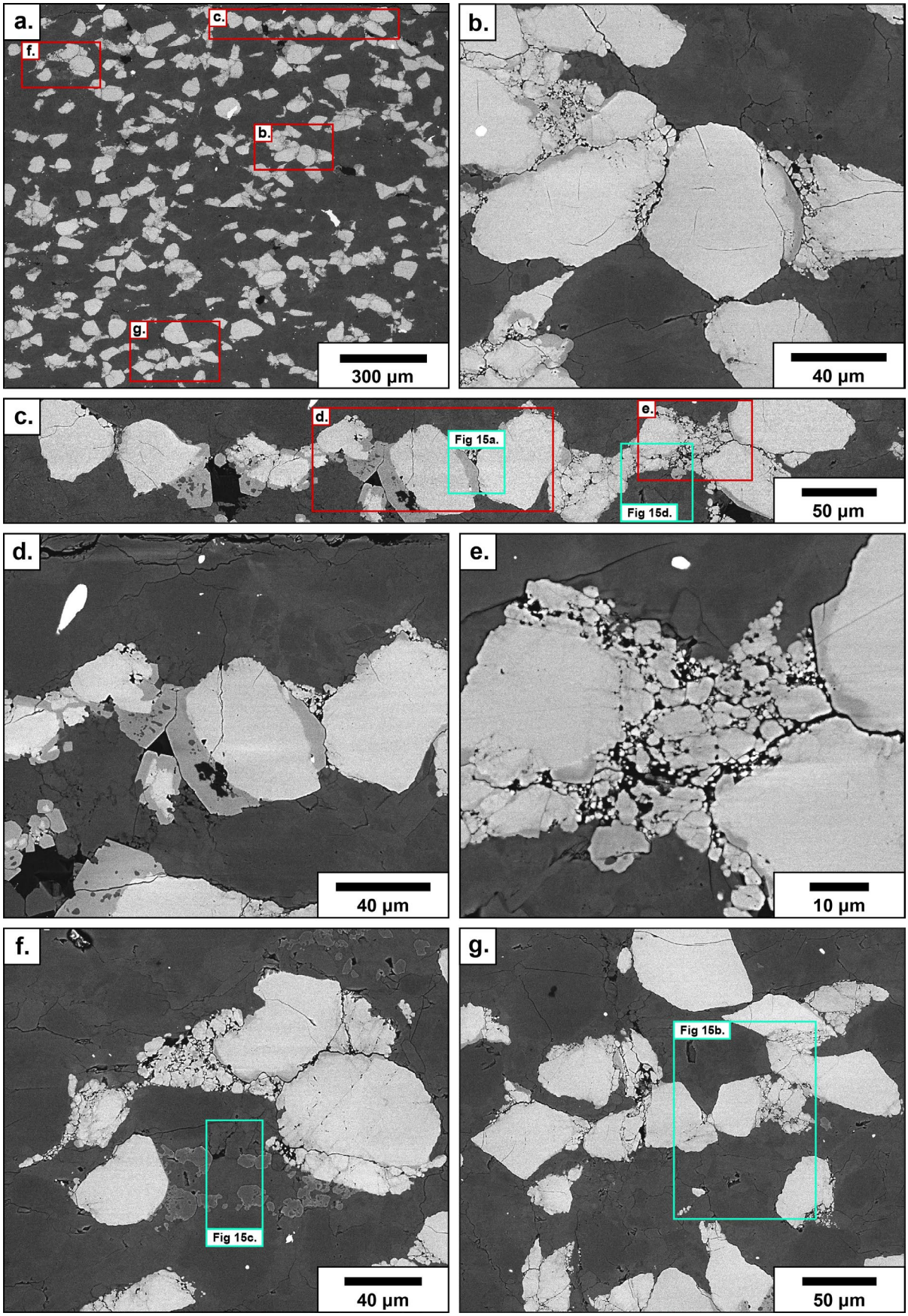

Figure 14: BSE images of sample PE04. Red rectangles mark the localities of close-ups, cyan rectangles mark localities of OC images. (a) Overview. (b) and (g) Garnet clusters with fractured contacts. (c) Horizontal garnet cluster with zoning and euhedral Mg-rich garnet crystals. (d) and (e) Close-ups of garnet-garnet contacts shown in (c). (f) Irregularly shaped, Mg-rich garnet crystals.

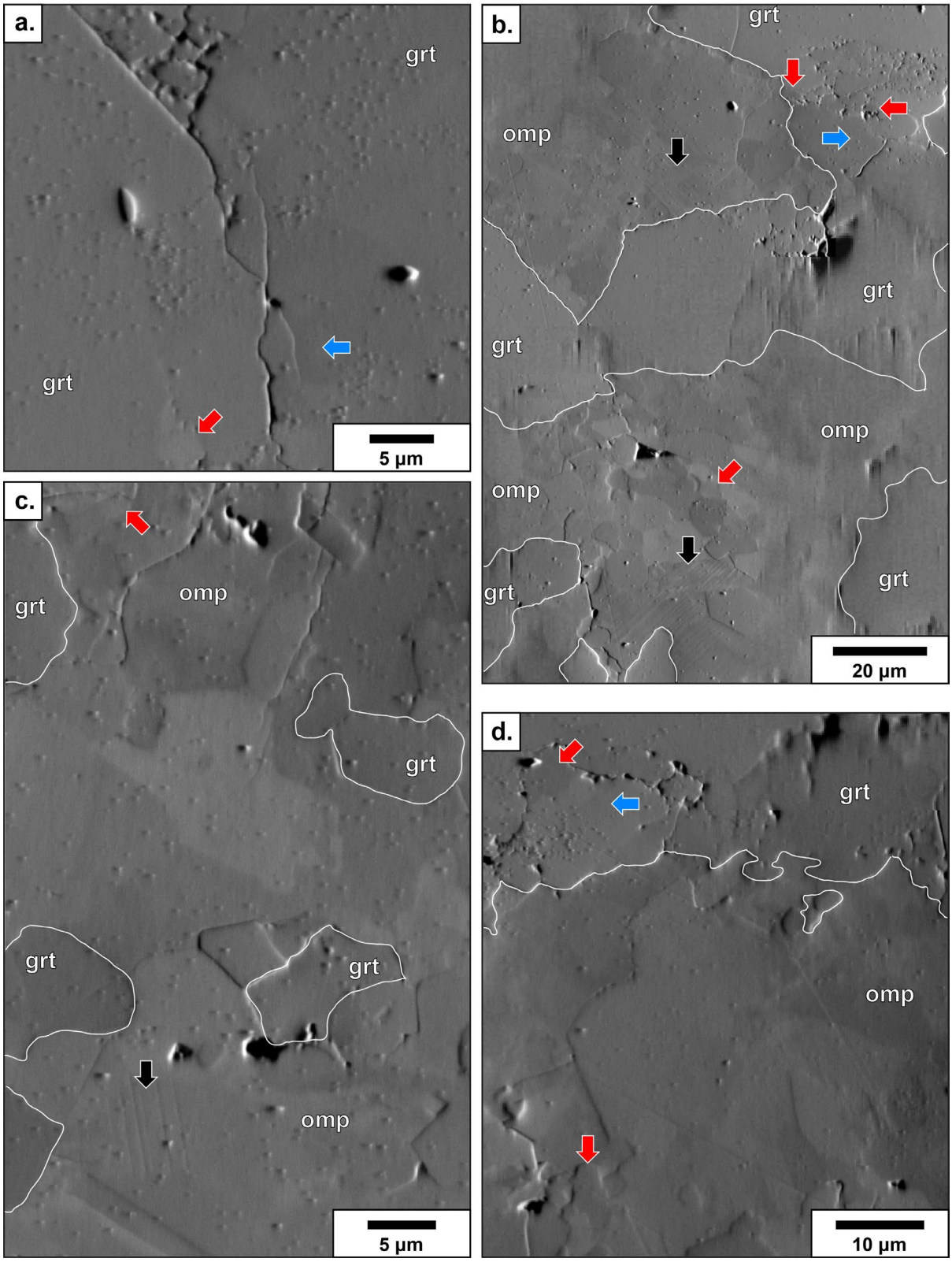

Figure 15: Orientation contrast mosaics of the slightly deformed sample (PE04). White borders mark interfaces between garnet and omphacite. The blue arrows point to gradual internal OC in garnet, the red arrows point to subgrains in both garnet and omphacite, and the black arrows point to deformation twins in omphacite. (a) Garnet gradual internal OC and subgrain next to intra-cluster grain boundary fracture. (b) Highly fractured garnet contacts revealing OC between fragments, subgrains and internal OC towards fractures; omphacite displays irregular internal OC, deformation twins and subgrains. The omphacite-rich domain in the lower part is cut by a fracture and exhibits a higher concentration of small euhedral crystals and subgrains. (c) Irregularly-shaped, Mg-rich garnet grains within fractured omphacite showing no internal OC; omphacite displays small euhedral crystals, slight internal OC, subgrains, and deformation twins. (d) Top: Highly fractured intra-cluster garnet-garnet contact with subgrains and internal OC; bottom: omphacite exhibits irregular internal OC and subgrains next to fracture.

4.2.4. PE02 (Maximum Compressive Strength – 7% Axial Strain)

The moderately deformed sample PE02 displays isometric garnet grains and garnet clusters with a slight tendency to align sub-horizontally; however, no persistent foliation is developed (Figure 9: PE02, Figure 16, Figure 17a). Microporosity, horizontal decompression cracks, and garnet/omphacite chemical zonations are observed, as well as Mg-enriched euhedral (Figure 17b) and irregular garnet crystals (Figure 17d). Fine-grained omphacite-rich domains with a grain size smaller than 10 µm are abundant in this sample (Figure 16, Figure 18), whereas larger crystals (50 – 100 µm) are less common (Figure 16). Garnet clusters consist of a few large grains (40 – 70 µm) surrounded by fragmented garnet material. The fragments are characterized by irregular shapes and sizes; down to a few micrometers (Figure 17d-e). Garnet clusters sometimes exhibit long, sub-horizontal fine-grained tails (Figure 17b).

Examination of omphacite in the BSE images indicates locally fracture-dense domains associated with fractured garnet clusters (Figure 17b and 17d). Optical microscope analysis suggests a weak SPO of omphacite, defined by elongated grains with deformation twins, undulatory extinction and subgrains (Figure 16). The OC images of omphacite display extensive fine-grained domains, which are often situated along fractures (Figure 18). These fine-grained domains are characterized by grains with rounded boundaries or euhedral crystals and exhibit a strong irregular OC and well-defined subgrains. Occasional deformation twins and grain boundary bulges are also observed. A large grain (> 100 µm) shown in the upper part of Figure 18b displays irregular grain boundaries and strong irregular internal OC and subgrains.

Garnet's examination through BSE imaging reveals isolated garnet grains that have straight to rounded boundaries and are often intact or slightly fractured. Garnet clusters exhibit a high fracture density, particularly towards garnet-garnet contacts, with vertical and randomly oriented fractures being abundant. Grain boundaries of intra-cluster garnets are angular or irregular, often originating from fractures (Figure 17b). An OC between garnet fragments, as well as substructures in the vicinity of fractures are observed in OC images. These substructures include irregular OC (Figure 18a), gradual OC towards fractures, and subgrains next to fractures (Figure 18).

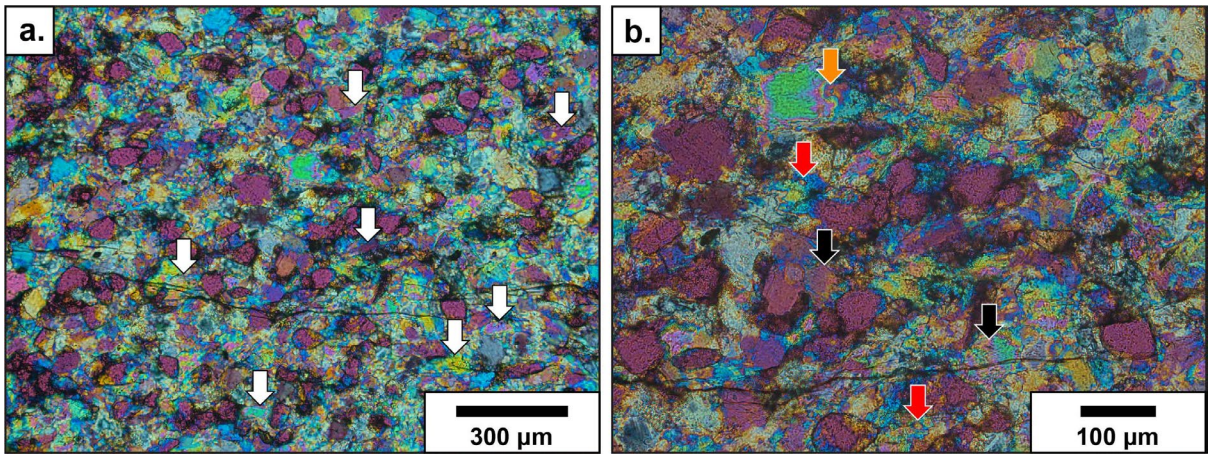

Figure 16: Optical photomicrographs of moderately deformed sample (PE02). Crossed polarizers and lambda plate inserted. White arrows point to elongated omphacite grains with undulatory extinction, black arrows point to twinned omphacite grains, red arrows point to omphacite subgrains, orange arrow points to omphacite grain boundary bulge.

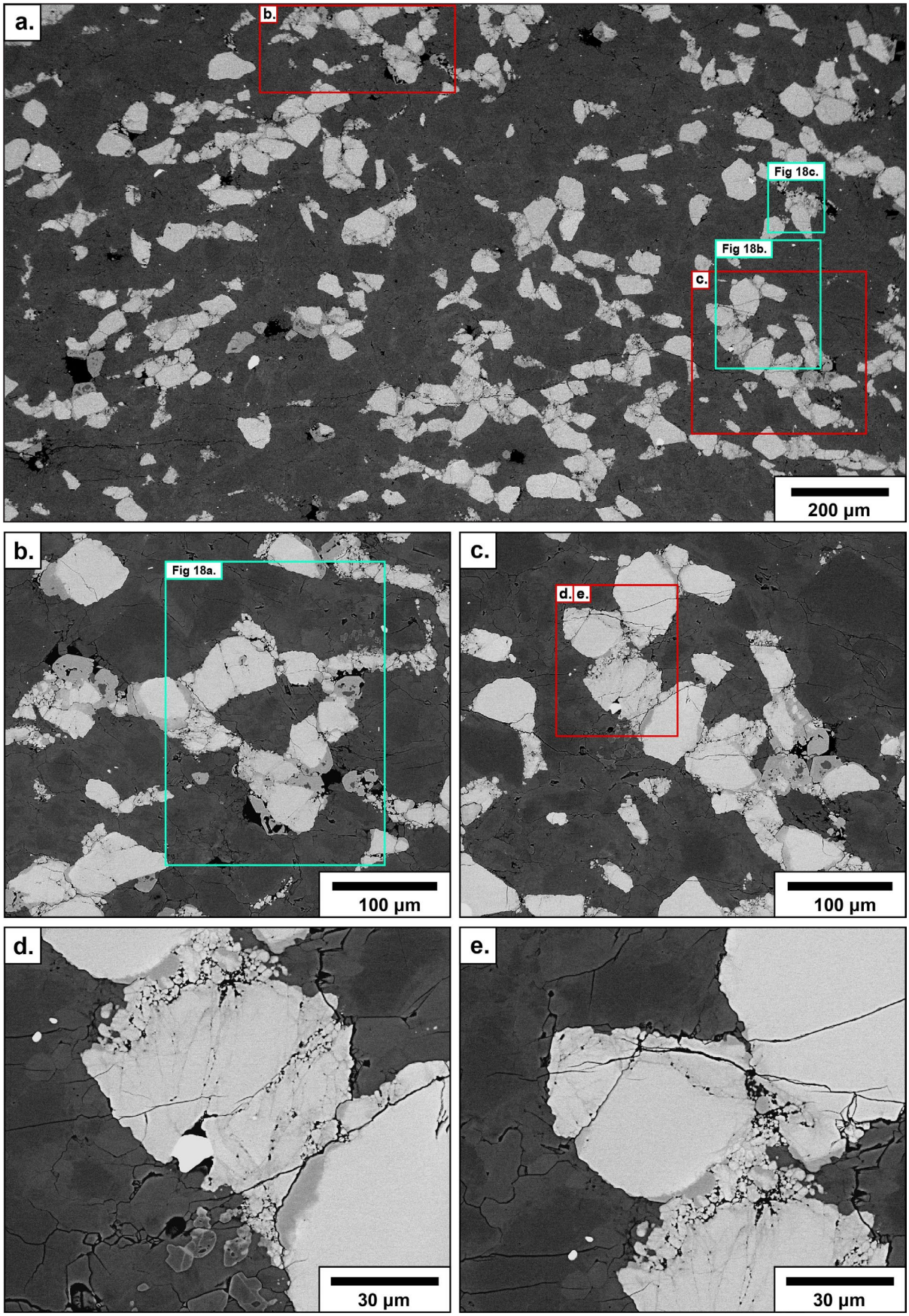

Figure 17: BSE images of sample PE02. Red rectangles mark the localities of subfigures, cyan rectangles mark OC domains. (a) Overview. (b) and (c) Garnet clusters with fractured contacts, chemical zoning, and euhedral crystals; (b) has sub-horizontal fine-grained tails. (d) and (e) Close-ups of garnet-garnet contacts of cluster (c). (d) Irregularly shaped garnet crystals along fracture.

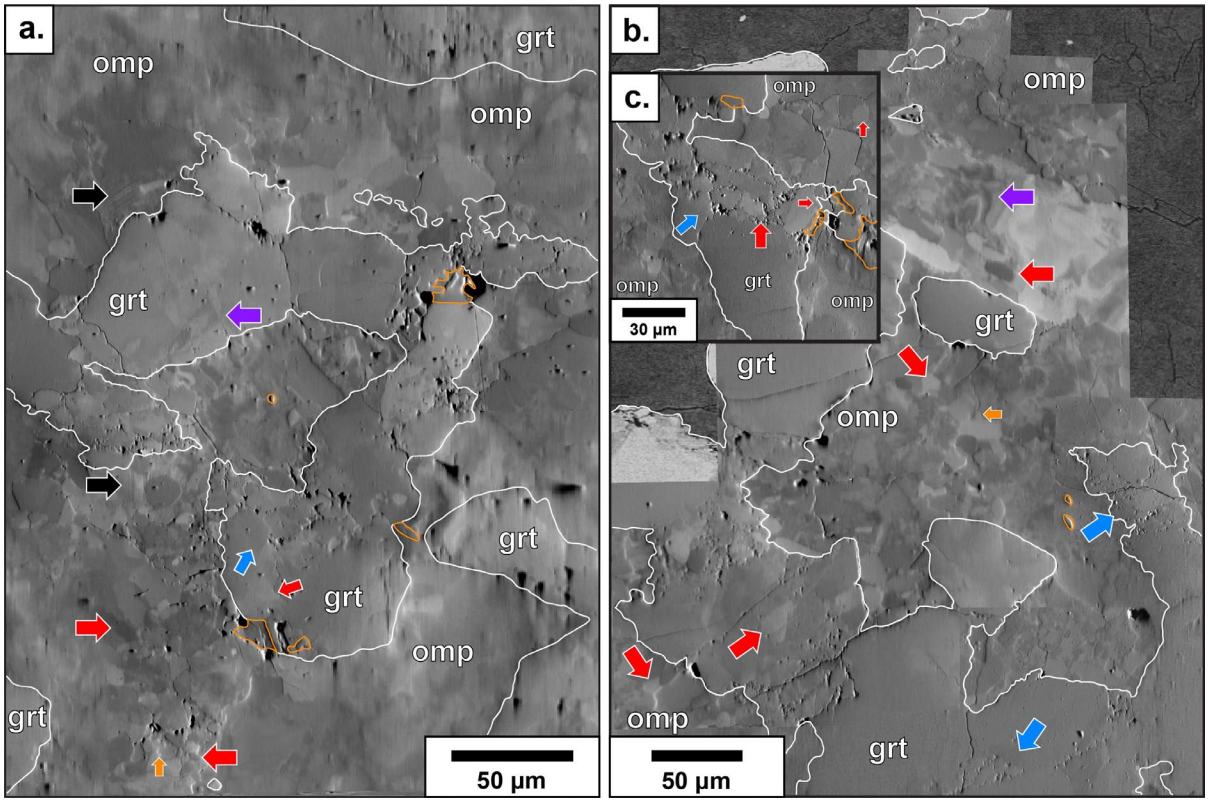

Figure 18: Orientation contrast mosaics of sample PE02; subfigure (b) OC mosaic is overlain on BSE micrograph. White borders mark interfaces between garnet and omphacite, orange boundaries mark grain boundaries of impurities. Blue arrows point to gradual internal OC in garnet, black arrows point to deformation twins in omphacite, orange arrows point to grain boundary bulges in omphacite. Purple arrows point to irregular orientation contrast in both phases, red arrows point to subgrains in both phases. (a) Garnet cluster with irregular internal OC, and fracture-dense domains with gradual internal OC and subgrains. Omphacite also displays irregular OC, twinned grains, and fine-grained domains with euhedral crystals, subgrains and bulges. (b) Highly fractured garnet cluster and fine-grained omphacite displaying features similar to (a); large omphacite grain with irregular OC in the upper right corner. (c) Highly fractured garnet cluster with subgrains, and fine-grained omphacite with euhedral grains and subgrains.

4.2.5. PE03 (High Axial Strain– Not Quantified (~42%))

The highly deformed sample PE03 is characterized by prevalent deformation microstructures and a significantly reduced grain size of both phases. The BSE overview mosaic demonstrates extensive brittle deformation features in both phases and a prevalent foliation, defined by flattened garnet clusters and elongated omphacite-rich domains arranged into layers (Figure 9: PE03). Both phases exhibit an SPO perpendicular to the maximum compressive stress (Figure 19, Figure 20a). Horizontal decompression cracks are only observed at the edges of the sample.

Analysis of omphacite in the BSE images shows brittle deformation associated with fractured garnet clusters; a higher fracture density occurs in narrow omphacite-rich domains squeezed in between garnet clusters (Figure 20e). Optical photomicrographs display abundant fine-grained domains (< 10 µm), often surrounding larger elongated grains (50 – 100 µm), which exhibit pronounced undulatory extinction and subgrains (Figure 19). Deformation twins are also observed throughout the sample. The OC image mosaic showed in Figure 22, displays a large omphacite grain in the lower part, exhibiting strong irregular internal OC and prevalent deformation twins. The large omphacite-rich domain displayed in the central part of Figure 22 is characterized by almost uniform orientations and minor irregular OC, suggesting a strong CPO.

BSE analysis of garnet reveals prevalent brittle deformation features throughout the sample; almost no garnet grains remained intact. Interestingly, even the large (40 – 70 µm), isolated garnet grains are heavily fractured and exhibit angular or irregular grain boundaries (Figure 21d); a few large grains are cut by oblique micro-faults (Figure 20b-c). The garnet clusters are flattened and exhibit extensive fragmentation by randomly-oriented fractures throughout their body; fragments are usually smaller than 10 µm (Figure 20d-e, Figure 21a-c). The grain boundaries of intra-cluster garnets are angular or irregular and originate from fractures. Clusters often have long tails with an extremely reduced grain size (< 1 µm), which are oriented parallel to the foliation plane (Figure 21b). An OC between garnet fragments, as well as subgrains next to fractures and gradual internal OC towards fractures are observed in OC images (Figure 22).

Chemical variations are observed in both omphacite and garnet, particularly along grain boundaries and healed fractures (Figure 20, Figure 21). The intermediately Mg-enriched variation of garnet appears either as sharply defined rims of grains, or as 'coronas' surrounding entire clusters (Figure 20b, Figure 21b). These rims and 'coronas' often have irregular grain boundaries and are usually fragmented (Figure 21b). Rarely, they extend into euhedral crystals (Figure 21c). The highly Mg-enriched variation of garnet manifests as irregularly-shaped crystals, which appear to extend from garnet rims along cracks within the omphacite matrix and do not display deformation features (Figure 20b).

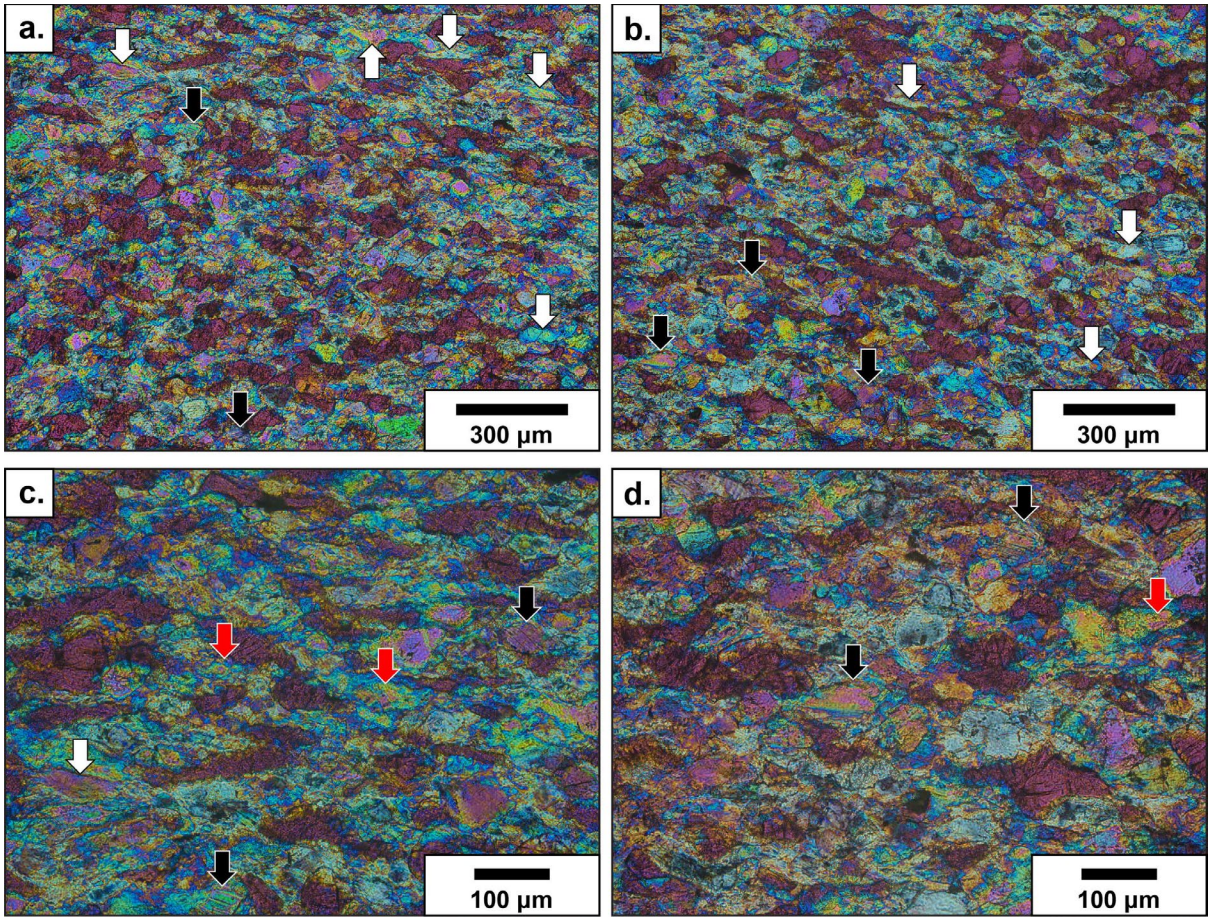

Figure 19: Optical photomicrographs of the highly deformed sample (PE03). Crossed polarizers and lambda plate inserted. Black arrows point to twinned omphacite grains, white arrows point to elongated omphacite grains with undulatory extinction, red arrows point to omphacite subgrains.

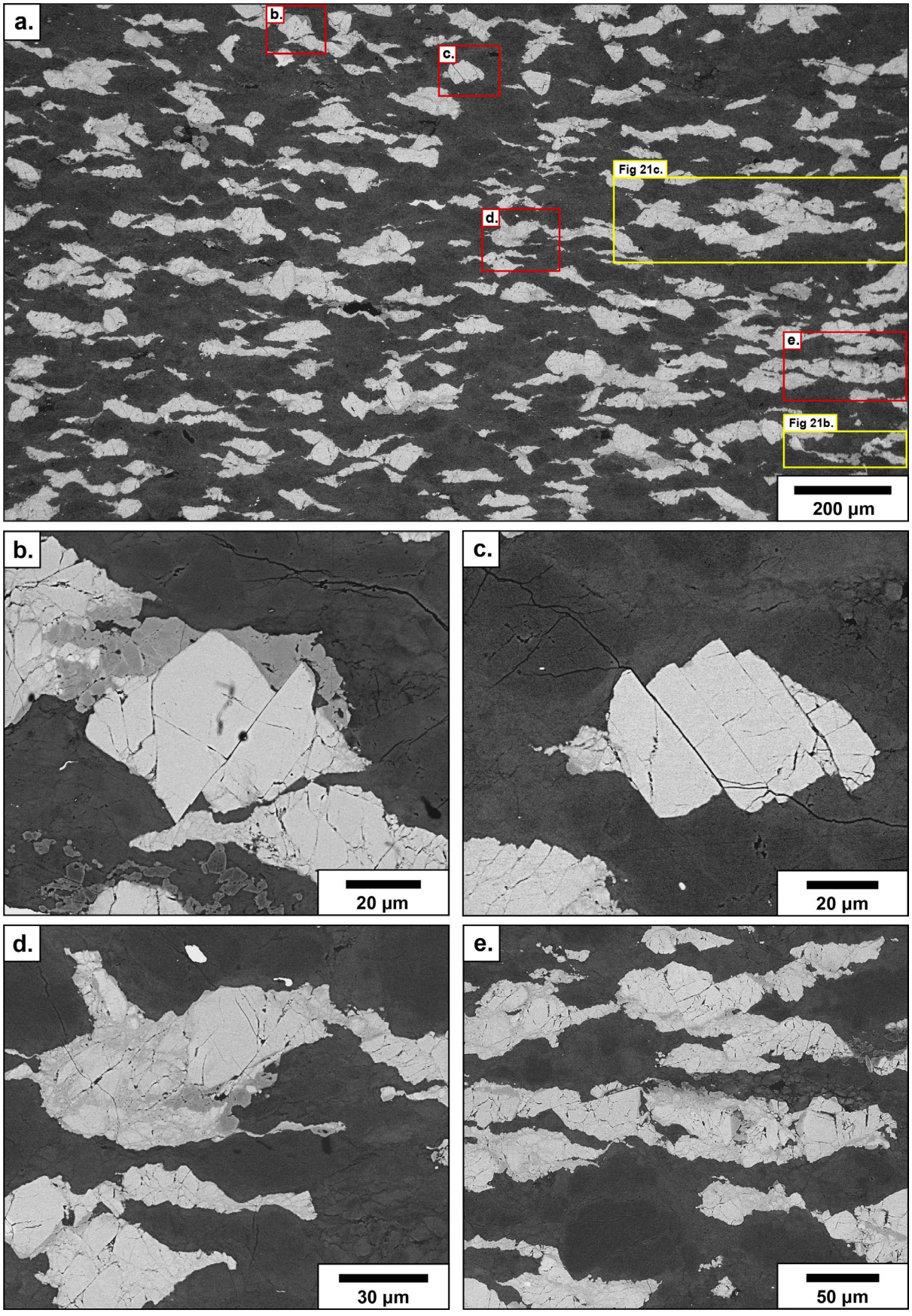

Figure 20: BSE images of sample PE03. The red rectangles mark the localities of close-ups, the yellow rectangles mark BSE mosaics in figure 21. (a) Overview. (b) Garnet cluster with micro-fault, intermediately Mg-enriched corona, and irregular Mg-rich garnet crystals. (b) Isolated garnet grain cut but micro-fault. (d) Highly fractured garnet cluster with Mg-enrichment along healed fractures. (e) Extensively fractured, flattened garnet clusters, and highly fractured omphacite-rich domain squeezed in between clusters.

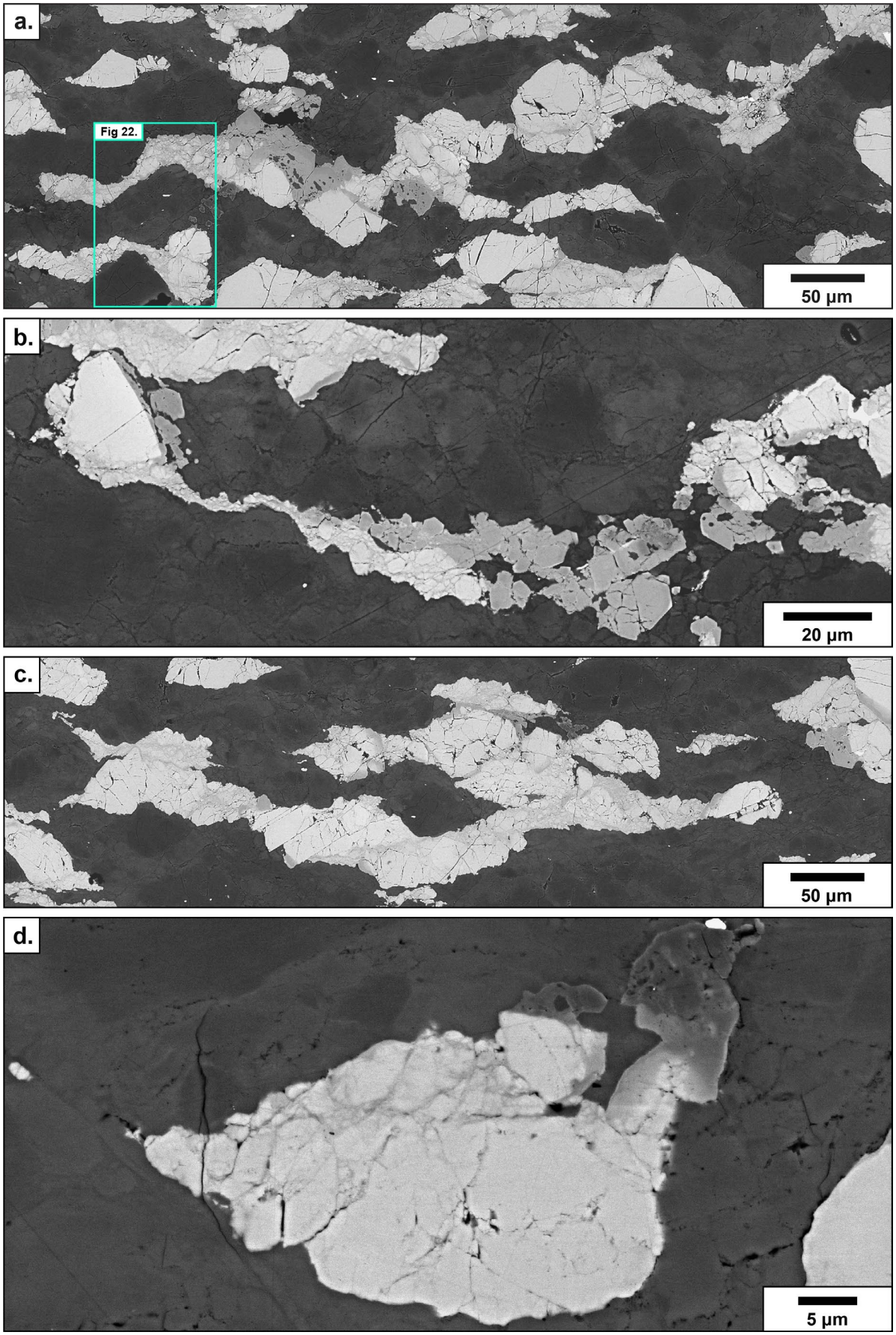

Figure 21: BSE image mosaics of sample PE03. The cyan rectangle marks OC images locality. (a) and (b) Garnet clusters with long, fine-grained tails and intermediately Mg-enriched coronas. (c) Elongated garnet cluster. (d) Highly fragmented isolated garnet grain.

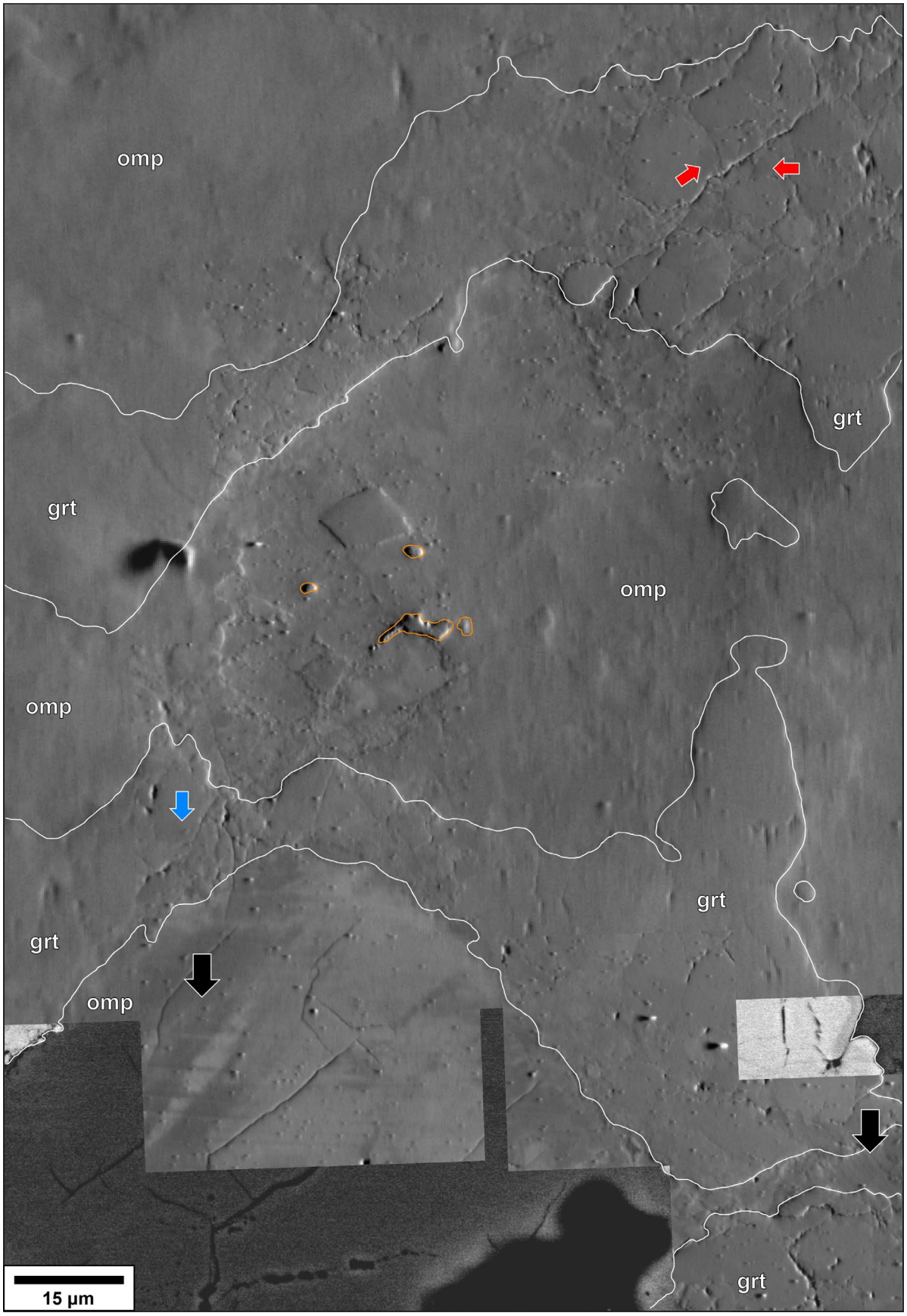

Figure 22: Orientation contrast mosaic overlain on BSE image of sample PE03. White borders mark interfaces between garnet and omphacite; orange borders mark grain boundaries of impurities. The blue arrow points to internal OC in garnet, the red arrows point to garnet subgrains, and the black arrow points to deformation twins in omphacite. The large omphacite-rich domain in the center appears with almost uniform orientations, indicating a strong CPO.

4.3. Quantitative Volume and 3D Interconnectivity Analysis

Table 3 summarizes the results of the quantitative 3D analyses conducted on the microtomographic data sets, derived by utilizing the label analysis operator in Avizo®. The table displays the results ordered by increasing strain, including the calculated volume fractions of garnet and omphacite, the interconnectivity of garnet and volume percentages of isolated garnet clusters derived from both the segmented and the 'eroded' data, and the volume reduction of garnet after the erosion operation (in percentage). The microtomographic data sets comprising the VOI, and visualizations of the modeled garnet volumes after the erosion operation are displayed in Appendix d.

Table 3: Quantitative volume and 3D interconnectivity data obtained by the label analysis operator in Avizo®.

Sample № (ϵ_{max})	Omphacite volume	Garnet volume	Garnet interconnectivity	Isolated garnet cluster volume	'Eroded' garnet volume reduction	'Eroded' garnet interconnectivity	'Eroded' isolated garnet cluster volume
PE01 (0%)	69.88%	24.25%	97.76%	2.24%	64.16%	87.46%	12.54%
PE04 (4.7%)	72.43%	24.23%	97.90%	2.10%	55.28%	92.51%	7.49%
PE02 (7%)	70.89%	24.06%	98.39%	1.61%	62.65%	89.12%	10.88%
PE03 (42%)	70.10%	24.88%	98.67%	1.33%	70.50%	84.05%	15.95%

Quantification of garnet's volume accounts for ~24 – 25% of the total volume of each modeled cube, and omphacite's volume approximates 70%. These values align with the volume fractions known from sample synthesis, albeit marginally reduced. The presence of unlabeled impurities and void volumes (~5% vol.) in the samples contributes to this decrease, detracting from the volumes of the primary labeled phases. Omphacite, being the most abundant phase, experiences a more drastic reduction in its modeled volume than garnet.

The results of garnet's interconnectivity analysis on the segmented data (without erosion) reveal that a single interconnected cluster accounts for at least 97% of garnet's total volume in all models. Interconnectivity increases slightly with increasing strain, which is in accord with the decreasing volume of isolated garnet clusters.

After subjecting the modeled garnet volumes to a single erosion step, the total garnet volume reduces dramatically (~55 – 70%). However, the total volume of garnet continues to be dominated by a single interconnected cluster, as garnet's high interconnectivity persists above ~84% in all models. Correlation of the results with strain shows an increase in 'eroded' interconnectivity from 87.46% in the undeformed state (PE01) to 92.51% at the yield point (PE04). This result is in accordance with the initial strain-dependent interconnectivity increase of the segmented data. In contrast to the results of the segmented data, the 'eroded' garnet interconnectivity shows a decrease past the yield point. Specifically, garnet's 'eroded' interconnectivity decreases to 89.12% at the maximum compressive strength point (PE02), and further decreases to 84.05% towards high strains (PE03). The strain-dependent evolution of the 'eroded' isolated garnet cluster volume correlates well with the evolution of the 'eroded' interconnectivity, showing an initial decrease from 12.54% in the undeformed state (PE01) to 7.49% at the yield point (PE04), followed by an increase to 10.88% at the maximum compressive strength point (PE02), and a further increase to 15.95% at high strain (PE03).

4.4. Quantitative 3D Shape Analysis

Table 4 summarizes the results of the fabric tensor calculations obtained through the Quant3D software by employing both the SVD and SLD methods. The 'eroded' segmented data were used for the calculations. The results are ordered by increasing strain and include the degree of shape anisotropy (DA) and the elongation index (E) of both garnet and omphacite. Additionally, the results of the SVD method are visualized in 3D rose diagrams in Figure 23.

Table 4: Degree of anisotropy (DA) and elongation index (E) of garnet and omphacite calculated with the SVD and SLD methods. The listed values are rounded averages derived from 10 iterations of the calculations.

	GARNET				OMPHACITE			
Sample № (ϵ_{max})	**SVD DA**	**SLD DA**	**SVD E**	**SLD E**	**SVD DA**	**SLD DA**	**SVD E**	**SLD E**
PE01 (0%)	1.6	1.2	0.1	0.0	1.6	1.2	0.1	0.0
PE04 (4.7%)	1.6	1.2	0.2	0.1	1.5	1.1	0.2	0.1
PE02 (7%)	1.6	1.2	0.1	0.0	1.7	1.2	0.1	0.0
PE03 (42%)	4.0	1.6	0.1	0.0	4.1	1.6	0.1	0.0

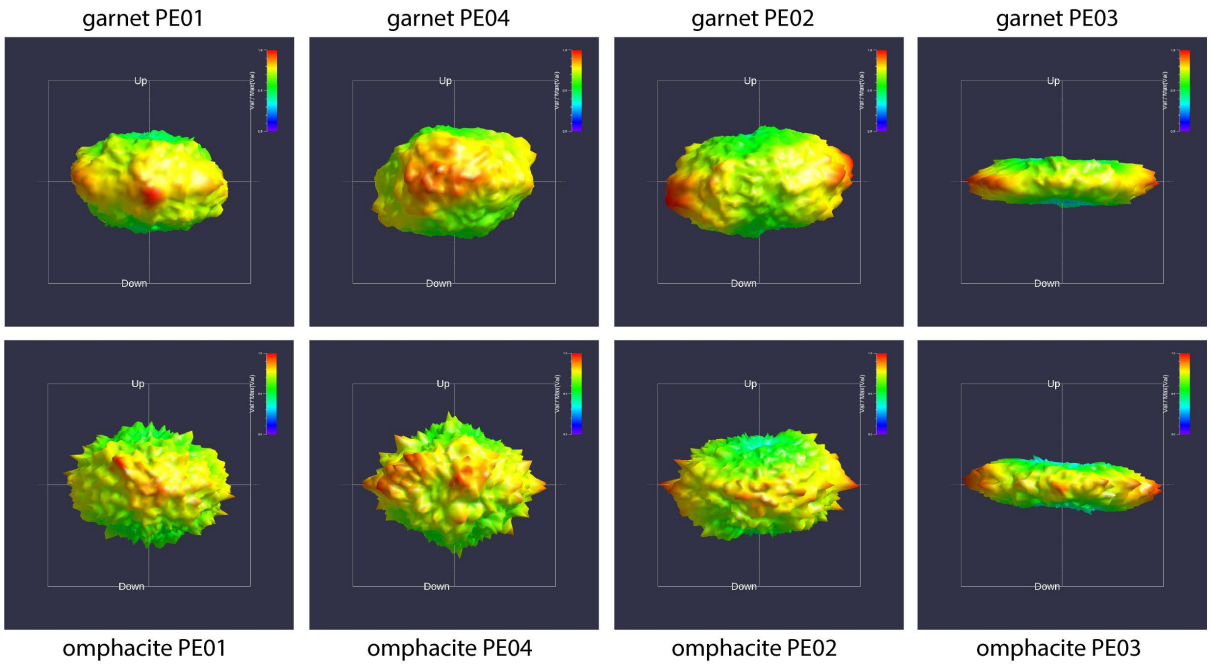

Figure 23: 3-dimensional rose diagrams depicting the results of the SVD method. The red regions indicate orientations with the strongest magnitudes (primary eigenvectors). The strongly oblate shapes of both phases at high strain (PE03) are contrasting the rose diagrams of the other samples.

The results show low degrees of anisotropy (DA) and elongation indexes (E) of both garnet and omphacite in the undeformed state (PE01) and at low to moderate strains (PE04, PE02), indicating randomly oriented or isotropic shapes rather than oriented oblate or elongated shapes. At high strain (PE03), both garnet and omphacite show strongly oblate shapes oriented perpendicular to the shortening direction (S-type fabric), indicated by high degrees of anisotropy and low elongation indexes. The elongation indexes of both phases show a minor peak at the yield point (PE04), and the degree of anisotropy of omphacite shows a slight dip, implying slight elongation at the yield point.

5. DISCUSSION

The deformation behavior of garnet and omphacite, the main constituents of eclogite, is fundamentally different under the applied deformation conditions (2.5 GPa, 900° C, $6.4 \cdot 10^{-6}$ s^{-1}), reflecting their contrasting rheological properties. Garnet grains primarily behave as rigid inclusions or deform in a brittle manner, whereas the omphacite matrix undergoes extensive intracrystalline deformation, even at low strains. This strain partitioning has been observed in both natural (e.g. Piepenbreier & Stöckhert, 2001; Kurz et al., 2004; Keppler et al., 2016) and experimentally deformed eclogites (e.g. Jin et al., 2001; Zhang & Green, 2007; Rogowitz et al., 2023) and is in accordance with theoretical and experimental studies on two-phase aggregates, which demonstrated that the weaker phase accommodates most of the strain (e.g. Jordan, 1987, Handy 1990; 1994). By systematically varying the duration of each deformation experiment in this study, the influence of total strain on the operative deformation mechanisms, the abundance of deformation microstructures, and the evolution of the microfabric has been evaluated.

5.1. Deformation Mechanisms

5.1.1. Garnet

Garnet predominantly deforms in a brittle manner in all experimental samples, with the degree of fragmentation and fracture orientation depending on the total strain and the spatial arrangement of grains. Numerical studies have demonstrated that stress concentrates at garnet-garnet contacts, leading to strain localization and local stress field perturbations in these regions (e.g. Yamato et al., 2019; Rogowitz et.al, 2023). In the undeformed sample (PE01), compaction during synthesis resulted in locally stress concentrated areas, as garnet exhibits evidence of cataclasis almost exclusively at garnet-garnet contacts. With a low to moderate strain increase (PE04, PE02), garnet clusters exhibit a higher fracture density, particularly at garnet-garnet contacts. The OC observed between fragments indicates rigid body rotation, which alongside the increasingly random orientation of fractures, indicate stress field perturbations. At high strain (PE03), extensive cataclasis is evident, as nearly all garnet grains are fragmented and the fracture density further increases, resulting in significant grain size reduction (down to < 1 μm).

Despite garnet's general resistance to dislocation activity, the experimental samples provide evidence for minor intracrystalline deformation. Even in the undeformed sample (PE01), lattice bending towards fractured garnet-garnet contacts is indicated by gradual internal OC. At low to moderate strains (PE04, PE02), lattice bending is more prevalent, and occasional subgrains occur next to fractured garnet-garnet contacts, as indicated by the sharp OC displayed in the images. At high strain (PE03), the occurrence of subgrains next to fractured garnet-garnet contacts is more prevalent. These observations suggest operation of dislocation glide even at very low strains, followed by operation of dislocation creep and recrystallization as strain accumulates. Garnet's intracrystalline deformation is evident exclusively in the vicinity of fractured garnet-garnet contacts (e.g. Voegelé et al., 1998). The reason for dislocation activity in these domains is the strain localization due to the locally increased stress concentration.

5.1.2. Omphacite

Omphacite deforms predominantly by intracrystalline deformation mechanisms, accompanied by cataclasis, which is indicated by fractures usually originating from heavily fractured garnet clusters. The dominant intracrystalline deformation mechanism depends on the total strain, as well as the spatial arrangement of the primary phases. Previous theoretical (Handy, 1990) and experimental studies on two-phase aggregates (Kenkmann & Dresen, 1998), and eclogites (Rogowitz et.al, 2023) have shown that stress concentrates within narrow zones of the weaker-phase matrix, leading to strain localization. The experimental samples examined in this study provide evidence to support these claims.

Even in the undeformed sample (PE01), compaction during synthesis resulted in locally stress concentrated areas. Large grains with undulatory extinction situated within narrow zones in between garnet clusters indicate the operation of dislocation glide (e.g. Godard & van Roermund, 1995). As strain increases to the yield point (PE04), dislocation creep begins to operate in stress concentrated areas. This is indicated by the elongation of omphacite grains situated in between garnet clusters, defining a weak SPO. The observation of fine-grained domains with euhedral omphacite crystals and well-defined subgrains adjacent to misoriented clasts is indicative of recrystallization (e.g. Keppler et al., 2016). The occurrence of recrystallized domains in the vicinity of fractures supports the suggestions of previous studies on experimental eclogites (Rogowitz et.al, 2023) and other naturally deformed rocks (e.g. Segall & Simpson, 1986), that brittle precursors promote the nucleation of recrystallized zones. The occasional deformation twins observed in the sample suggest concomitant mechanical twinning. As strain further increases to the maximum compressive strength point (PE02), features indicative of dislocation creep and recrystallization become more widespread, while mechanical twinning continues to operate in the background. Recrystallized zones surrounding fractured omphacite-rich domains are more extensive in this sample. At high strains (PE03), the entire omphacite matrix undergoes intracrystalline deformation accompanied by significant brittle deformation. Large crystals are always elongated, resulting in a persistent SPO, and they display strong undulatory extinction, deformation twins, and subgrains. Fine-grained domains are abundant, indicating significant grain size reduction. The fine-grained domains often surround larger grains, while also being elongated and contributing to the SPO. These features are indicative of recrystallization. The OC analyzed domain displays an almost uniform OC, implying a strong CPO. The prevalent recrystallization features alongside the strong CPO suggest dislocation creep and recrystallization dominance (e.g. Godard & van Roermund, 1995). Brittle deformation of omphacite in this sample is induced by fractures originating in the heavily fragmented garnet clusters; the stress concentrated, narrow omphacite-rich domains situated in between garnet clusters promote fracturing, resulting in locally increased fracture density.

In summary, stress concentrated domains in the omphacite matrix promote minor dislocation activity operating by glide, even at no induced deformation. At low to moderate strains, dislocation creep begins operating, with recrystallized zones nucleating around fractures. At high strains, dislocation creep and recrystallization dominate, accompanied by significant cataclasis; stress concentrated zones promote extensive fracturing.

5.2. Microfabric Evolution

The strain-dependent evolution of the microfabric of experimentally deformed synthetic dry eclogites has been assessed in this study. SEM analysis indicates that the onset of foliation development initiates at low to moderate strains, as omphacite develops a weak SPO and garnet grains occasionally tend to cluster and arrange sub-horizontally in the samples representing both the yield point (PE04), and maximum compressive strength point (PE02). Nevertheless, only the highly strained sample (PE03) displays a fully developed foliation. The foliation is defined by a persistent SPO of both omphacite and garnet clusters, which are arranged in layers. This observation suggests that a foliation fully develops only if deformation surpasses the point of maximum compressive strength.

The quantitative analysis of garnet and omphacite's 3D shapes with the Quant3D software aligns well with the SEM microfabric analysis. The results of the 3D shape analysis revealed that a prominent shape fabric develops only beyond the point of maximum compressive strength, as the three low-deformation samples exhibit random shape fabrics. The high degrees of anisotropy and low elongation indexes calculated for both garnet and omphacite at high strain (PE03), indicate strongly oblate shapes, which define a prominent S-type fabric. The layering of garnet and omphacite, observed under the SEM at high strain, is in accordance with the S-type fabric calculated by Quant3D.

The quantitative interconnectivity analysis of the segmented data with Avizo® revealed a very high interconnectivity of garnet clusters at all strain levels (> 97%). The fact that the high interconnectivity persists after the numerical erosion operation at all strain levels (> 84%) suggests that the interconnectivity of garnet is founded on strong cluster connections (e.g. Macente et al., 2017). Analysis of the strain-dependent evolution of garnet's interconnectivity, using the segmented data, showed a positive correlation between strain and interconnectivity. This strain-dependent increase of garnet's interconnectivity aligns with the general observations of foliation development with increasing strain. However, the results of the interconnectivity analysis, using the 'eroded' data, are in discord with the analysis of the segmented data. The 'eroded' data showed an initial increase in interconnectivity until the yield point (PE04), followed by a continuous decrease towards higher strains (PE02, PE03). The initial increase in 'eroded' interconnectivity suggests that garnet clustering is initiating at the yield point without significant segregation into layers. The subsequent, gradual decrease in 'eroded' interconnectivity suggests that foliation development past the yield point segregates garnet into layers. While interconnectivity might constantly increase within the foliation plane, the cluster connections between layers weaken, resulting in a reduction in the 3D interconnectivity of garnet as the layered clusters become separated perpendicular to the foliation plane.

In summary, garnet initiates clustering and omphacite begins to elongate at low strains, segregation of the primary phases into layers initiates around the point of maximum compressive strength, and a fully developed, S-type foliation forms beyond that point. In an attempt to provide a more intuitive perspective on the strain-dependent microfabric evolution, Figure 24 presents visualizations of garnet subvolumes, modeled in Avizo®, alongside 3D rose diagrams of the shape fabric tensors of garnet, calculated with the Quant3D software.

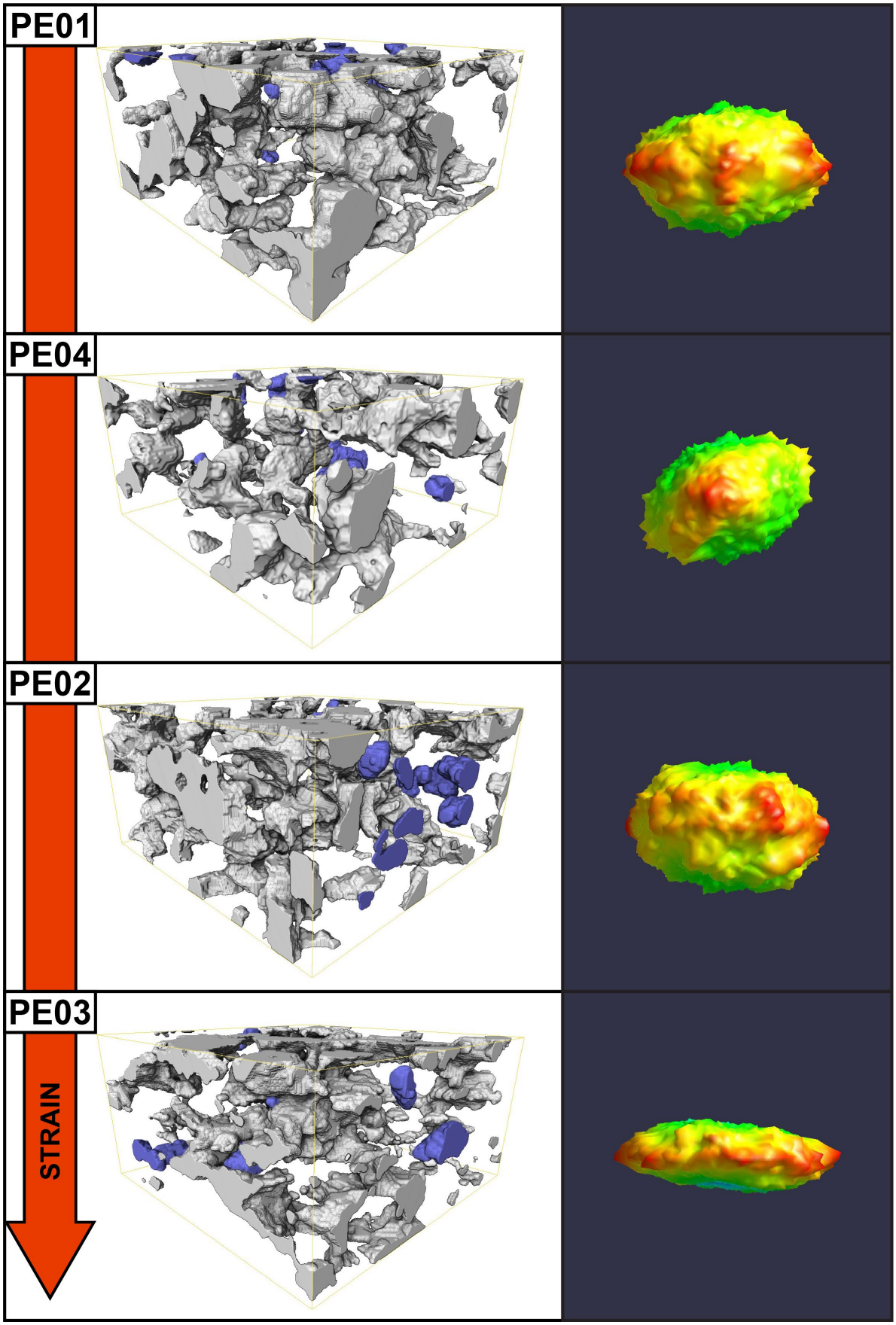

Figure 24: Left: Visualizations of parallelepipeds (0.5×0.5×0.25 mm) extracted from the modeled volumes of garnet, generated with the volume rendering operator in Avizo®. The interconnected garnet clusters are gray, and the isolated garnet clusters are purple. Right: 3D rose diagrams of garnet's SVD fabric tensors. The red regions indicate orientations with the strongest magnitudes.

5.3. Chemical Variations of Garnet and Omphacite

The chemical variations of garnet and omphacite, which have been observed in all samples, suggest non-equilibrium conditions for the particular modal compositions used in the experiments, and indicate the operation of diffusive mass transfer mechanisms (e.g. Stünitz et al., 2020). Fractures and phase boundaries appear to facilitate diffusion.

In the undeformed and the low/moderate-strain samples (PE01, PE04, PE02), the chemical variations manifest as zonations of both garnet and omphacite, whereas garnet also experiences crystal growth. The Mg-enriched garnet rims are interpreted to diffuse into the microporosity, forming moderately Mg-enriched euhedral garnet crystals, and diffuse into cracks within the omphacite matrix, forming highly Mg-enriched irregular garnet crystals. Both of these types of crystals are interpreted to begin growing during synthesis, as they are evident in sample PE01, and continue to grow during moderate deformation, as they do not display deformation features in samples PE04 and PE02.

In the highly deformed sample (PE03), the chemical variations are commonly observed along healed fractures in both garnet and omphacite. Mg-enriched euhedral garnet crystals are very uncommon in this sample. Instead, large domains consisting of the intermediately Mg-enriched garnet variation form 'coronas' surrounding entire clusters. These 'coronas' are often fragmented, suggesting that the rate of cataclasis of garnet surpassed the rate of diffusion of this particular garnet variation. The irregularly-shaped garnet crystals, which are highly enriched in Mg, are often undeformed in sample PE03, suggesting that the diffusion of garnet material that is highly enriched in Mg continued at a rate higher than the rate of cataclasis of the omphacite matrix, even at high strains. Another possible explanation is that the high-Mg variation of garnet continued to grow after the deformation had stopped, possible during the decompression/cooling phase of the experiment.

6. CONCLUSIONS

Axial compression experiments on synthetic dry eclogites with a composition of 75% omphacite – 25% garnet, performed in a Griggs-type deformation apparatus at 2.5 GPa, 900° C, $6.4 \cdot 10^{-6}$ s^{-1}, provided insights on the strain-dependent evolution of their microfabric and the operative deformation mechanisms. The conclusions have been derived by associating the quantitative mechanical data from the deformation experiments with analyses of the microfabrics, which were performed in both 2D and 3D, using SEM imaging and micro CT respectively. The main findings include:

- The yield point of synthetic dry eclogites with a composition of 75% omphacite – 25% garnet deformed at 2.5 GPa, 900° C, $6.4 \cdot 10^{-6}$ s^{-1} is reached at ~5% total strain, and the point of maximum compressive strength is reached at ~7% total strain.
- The deformation behavior of garnet and omphacite differs at the given conditions; garnet either remains rigid or deforms in a brittle manner, while omphacite deforms predominately by intracrystalline deformation mechanisms.
- Stress concentrated zones, such as intra-cluster garnet-garnet contacts and narrow omphacite-rich zones situated in between garnet clusters promote strain localization. Nucleation of recrystallized zones in omphacite is promoted by fractures originating from garnet clusters.
- Although garnet is generally resistant to intracrystalline deformation, increasing strain results locally in minor dislocation activity in the vicinity of fractures.
- Total strain influences the abundance of deformation microstructures observed in both primary phases, and the dominant intracrystalline deformation mechanism in omphacite. Low strains (< 5%) cause omphacite to glide, and higher strains activate dislocation creep and recrystallization.

The strain-dependent analysis of the evolution of the microfabric concluded that the total strain influences various aspects of the microfabric, including foliation development, the shape tensors of both omphacite and the garnet clusters, and garnet's interconnectivity:

- Foliation development initiates at the yield point, with garnet clustering and elongation of omphacite crystals. Segregation into layers begins at the point of maximum compressive strength. A fully developed foliation, defined by distinct layers, forms only beyond the point of maximum compressive strength.
- The shape fabric of both garnet clusters and omphacite is developed beyond the point of maximum compressive strength, resulting in prevalent oblate shapes, which define an S-type shape fabric.
- The interconnectivity of garnet clusters increases as strain accumulates up to the yield point. Further deformation results in a gradual decrease in interconnectivity, as clusters are segregated into distinct layers.

REFERENCES

Agard, P., Plunder, A., Angiboust, S., Bonnet, G., & Ruh, J. (2018). The subduction plate interface: Rock record and mechanical coupling (from long to short timescales). *Lithos*, 320, 537–566. https://doi.org/10.1016/j.lithos.2018.09.029

Agard, P., Prigent, C., Soret, M., Dubacq, B., Guillot, S., & Deldicque, D. (2020). Slabitization: Mechanisms controlling subduction development and viscous coupling. *Earth-Science Reviews*, 208, 103259. https://doi.org/10.1016/j.earscirev.2020.103259

Allen, F. M., Smith, B. K. & Buseck, P. R. (1987). Direct observation of dissociated dislocations in garnet. *Science*, 238(4834), 1695–1697. https://doi.org/10.1126/science.238.4834.1695

Angiboust, S., Agard, P., Raimbourg, H., Yamato, P., & Huet, B. (2011). Subduction interface processes recorded by eclogite-facies shear zones (Monviso, W. Alps). *Lithos*, 127(1–2), 222–238. https://doi.org/10.1016/j.lithos.2011.09.004

Arganda-Carreras, I., Kaynig, V., Rueden, C., Eliceiri, K. W., Schindelin, J., Cardona, A., & Sebastian Seung, H. (2017). Trainable Weka Segmentation: a machine learning tool for microscopy pixel classification. *Bioinformatics*, 33(15), 2424–2426. https://doi.org/10.1093/bioinformatics/btx180

Austrheim, H., (2013). Fluid and deformation induced metamorphic processes around Moho beneath continent collision zones: examples from the exposed root zone of the Caledonian mountain belt, W-Norway. *Tectonophysics*, 609, 620–635. https://doi.org/10.1016/j.tecto.2013.08.030

Austrheim, H. & Boundy, T. M. (1994). Pseudotachylytes generated during seismic faulting and eclogitization of the deep crust. *Science*, 265(5168), 82–83. https://doi.org/10.1126/science.265.5168.82

Austrheim, H., Dunkel, K. G., Plümper, O., Ildefonse, B., Liu, Y., & Jamtveit, B. (2017). Fragmentation of wall rock garnets during deep crustal earthquakes. *Science Advances*, 3(2), e1602067. https://doi.org/10.1126/sciadv.1602067

Bascou, J., Barruol, G., Vauchez, A., Mainprice, D., & Egydio-Silva, M. (2001). EBSD-measured lattice-preferred orientations and seismic properties of eclogites. *Tectonophysics*, 342(1–2), 61–80. https://doi.org/10.1016/s0040-1951(01)00156-1

Bestmann, M., Habler, G., Heidelbach, F., & Thöni, M. (2008). Dynamic recrystallization of garnet and related diffusion processes. *Journal of Structural Geology*, 30(6), 777–790. https://doi.org/10.1016/j.jsg.2008.02.007

Bird, P. (1979). Continental delamination and the Colorado Plateau, *Journal of Geophysical Research: Solid Earth*, 84(B13), 7561–7571. https://doi.org/10.1029/JB084iB13p07561

Blenkinsop, T. (2000). *Deformation Microstructures and Mechanisms in Minerals and Rocks*. Springer Dordrecht. https://doi.org/10.1007/0-306-47543-X

Boundy, T. M., Fountain, D. M., Austrheim, H., (1992). Structural development and petrofabrics of eclogite facies shear zones, Bergen Arcs, western Norway: implications for the deep crustal deformation processes. *Journal of Metamorphic Geology*, 10(2), 127–146. https://doi.org/10.1111/j.1525-1314.1992.tb00075.x

Broadwell, K. S., Locatelli, M., Verlaguet, A., Agard, P., & Caddick, M. J. (2019). Transient and periodic brittle deformation of eclogites during intermediate-depth subduction. *Earth and Planetary Science Letters*, 521, 91–102. https://doi.org/10.1016/j.epsl.2019.06.008

Burov, E., Francois, T., Agard, P., Le Pourhiet, L., Meyer, B., Tirel, C., Lebedev, S., Yamato, P., Brun, J.-P. (2014). Rheological and geodynamic controls on the mechanisms of subduction and HP/UHP exhumation of crustal rocks during continental collision: Insights from numerical models. *Tectonophysics*, 631, 212–250. https://doi.org/10.1016/j.tecto.2014.04.033

Chen, I. W., & Molnar, W. P. (1983). Focal depths of intracontinental and intraplate earthquakes and their implications for the thermal and mechanical properties of the lithosphere. *Journal of Geophysical Research: Solid Earth*, 88(B5), 4183–4214. https://doi.org/10.1029/JB088iB05p04183

Coleman, R. G., Lee, D. E., Beatty, L. B., Brannock, W. W. (1965). Eclogites and Eclogites: Their differences and Similarities, *Geological Society of America Bulletin*, 76(5), 483–508. https://doi.org/10.1130/0016-7606(1965)76[483:EAETDA]2.0.CO;2

De Bresser, J. H., Ter Heege, J. H., Spiers, C. J. (2001). Grain size reduction by dynamic recrystallization: can it result in major rheological weakening? *International Journal of Earth Sciences*, 90, 28–45. https://doi.org/10.1007/s005310000149

Dierick, M., Masschaele, B., Van Hoorebeke, L. (2004). Octopus, a fast and user-friendly tomographic reconstruction package developed in LabView®. *Measurement Science and Technology*, 15(7), 1366–1370. https://doi.org/10.1088/0957-0233/15/7/020

Druiventak, A., Trepmann, C. A., Renner, J., & Hanke, K. (2011). Low-temperature plasticity of olivine during high stress deformation of peridotite at lithospheric conditions - An experimental study. *Earth and Planetary Science Letters*, 311(3–4), 199–211. https://doi.org/10.1016/j.epsl.2011.09.022

Engvik, A.K., Austrheim, H., Erambert, M., (2001). Interaction between fluid flow, fracturing and mineral growth during eclogitization, and example from the Sunnfjord area, Western Gneiss Region, Norway. *Lithos*, 57 (2–3), 111–141. https://doi.org/10.1016/S0024-4937(01)00037-8

Fusseis, F., Regenauer-Lieb, K., Liu, J., Hough, R.M., De Carlo, F., (2009). Creep cavitation can establish a dynamic granular fluid pump in ductile shear zones. *Nature*, 459(7249), 974–977. https://doi.org/10.1038/nature08051

Fusseis, F., Schrank C., Liu, J., Karrech, A., Llana-F´unez, S., Xiao, X., and Regenauer-Lieb, K. (2012). Pore formation during dehydration of a polycrystalline gypsum sample observed and quantified in a time-series synchrotron X-ray micro-tomography experiment. *Solid Earth*, 3(1), 71–86. https://doi.org/10.5194/se-3-71-2012

Godard, G., & van Roermund, H. L. (1995). Deformation-induced clinopyroxene fabrics from eclogites. *Journal of Structural Geology*, 17(10), 1425–1443. https://doi.org/10.1016/0191-8141(95)00038-f

Green, D. H., & Ringwood, A. E. (1967). An experimental investigation of the gabbro to eclogite transformation and its petrological applications. *Geochimica et Cosmochimica Acta*, 31(5), 767–833. https://doi.org/10.1016/s0016-7037(67)80031-0

Griggs, D. (1967). Hydrolytic weakening of quartz and other silicates. *Geophysical Journal International*, 14(1–4), 19–31. https://doi.org/10.1111/j.1365-246x.1967.tb06218.x

Hacker, B. R., Kelemen, P. B., & Behn, M. D. (2015). Continental lower crust. *Annual Review of Earth and Planetary Sciences*, 43(1), 167–205. https://doi.org/10.1146/annurev-earth-050212-124117

Hacker, B. R., Peacock, S. M., Abers, G. A. & Holloway, S. D. (2003). Subduction factory – 2. Are intermediate-depth earthquakes in subducting slabs linked to metamorphic dehydration reactions? *Journal of Geophysical Research*: *Solid Earth*, 108(B1). https://doi.org/10.1029/2001JB001129

Handy, M. R. (1990). The solid-state flow of polymineralic rocks. *Journal of Geophysical Research: Solid Earth*, 95(B6), 8647–8661. https://doi.org/10.1029/jb095ib06p08647

Handy, M. R. (1994). Flow laws for rocks containing two non-linear viscous phases: A phenomenological approach. *Journal of Structural Geology*, 16(3), 287–301. https://doi.org/10.1016/0191-8141(94)90035-3

Hertgen, S., Yamato, P., Morales, L. F. G., & Angiboust, S. (2017). Evidence for brittle deformation events at eclogite-facies P-T conditions (example of the Mt. Emilius klippe, Western Alps). *Tectonophysics*, 706–707, 1–13. https://doi.org/10.1016/j.tecto.2017.03.028

Huet, B., Yamato, P., & Grasemann, B. (2014). The Minimized Power Geometric model: An analytical mixing model for calculating polyphase rock viscosities consistent with experimental data. *Journal of Geophysical Research: Solid Earth*, 119(4), 3897–3924. https://doi.org/10.1002/2013jb010453

Incel, S. (2017). *Experimental constraints on rheology during eclogite-facies metamorphic reactions* (PhD Thesis). Université Paris sciences et lettres. https://tel.archives-ouvertes.fr/tel-01628809

Ji, S., Saruwatari, K., Mainprice, D., Wirth, R., Xu, Z., & Xia, B. (2003). Microstructures, petrofabrics and seismic properties of ultra high-pressure eclogites from Sulu region, China: Implications for rheology of subducted continental crust and origin of mantle reflections. *Tectonophysics*, 370(1–4), 49–76. https://doi.org/10.1016/s0040-1951(03)00177-x

Ji, S., Zhao, P., Xia, B. (2003). Flow laws of multiphase materials and rocks from endmember flow laws. *Tectonophysics*, 370(1–4), 129–145. https://doi.org/10.1016/S0040-1951(03)00182-3

Jin, Z. M., Zhang, J., Green, H. W., & Jin, S. (2001). Eclogite rheology: Implications for subducted lithosphere. *Geology*, 29(8), 667–670. https://doi.org/10.1130/0091-7613(2001)029<0667:erifsl>2.0.co;2

Jolivet, L., Raimbourg, H., Labrousse, L., Avigad, D., Leroy, Y., Austrheim, H., & Andersen, T. B. (2005). Softening trigerred by eclogitization, the first step toward exhumation during continental subduction. *Earth and Planetary Science Letters*, 237(3–4), 532–547. https://doi.org/10.1016/j.epsl.2005.06.047

Jordan, P. G. (1987). The deformational behaviour of bimineralic limestone-halite aggregates. *Tectonophysics*, 135(1–3), 185–197. https://doi.org/10.1016/0040-1951(87)90160-0

Jordan, P. G. (1988). The rheology of polymineralic rocks: an approach. *Geologische Rundschau*, 77(1), 285–294. https://doi.org/10.1007/BF01848690

Karato, S., Wang, Z., Liu, B. & Fujino, K. (1995). Plastic deformation of garnets: systematics and implications for the rheology of the mantle transition zone. *Earth and Planetary Science Letters*, 130(1–4), 13–30. https://doi.org/10.1016/0012-821X(94)00255-W

Katayama, I., & Karato, S. I. (2008). Effects of water and iron content on the rheological contrast between garnet and olivine. *Physics of the Earth and Planetary Interiors*, 166(1–2), 57–66. https://doi.org/10.1016/j.pepi.2007.10.004

Kenkmann, T., & Dresen, G. (1998). Stress gradients around porphyroclasts: Palaeopiezometric estimates and numerical modelling. *Journal of Structural Geology*, 20(2–3), 163–173. https://doi.org/10.1016/s0191-8141(97)00074-6

Keppler, R., Stipp, M., Behrmann, J. H., Ullemeyer, K., & Heidelbach, F. (2016). Deformation inside a paleosubduction channel–insights from microstructures and crystallographic preferred orientations of eclogites and metasediments from the Tauern Window, Austria. *Journal of Structural Geology*, 82, 60–79. https://doi.org/10.1016/j.jsg.2015.11.006

Ketcham, R. A. & Ryan, T. M. (2004). Quantification and visualization of anisotropy in trabecular bone. *Journal of Microscopy*, 213(2), 158–171. https://doi.org/10.1111/j.1365-2818.2004.01277.x

Kirby, S. H., Engdahl, E. R. & Denlinger, R. P. (1996). Intermediate-depth intraslab earthquakes and arc volcanism as physical expressions of crustal and uppermost mantle metamorphism in subducting slabs. In *Subduction Top to Bottom*, *Geophysical Monograph*, 96, (pp. 195–214). https://doi.org/10.1029/GM096p0195

Kurz, W., Jansen, E., Hundenborn, R., Pleuger, J., Schäfer, W., & Unzog, W. (2004). Microstructures and crystallographic preferred orientations of omphacite in Alpine eclogites: Implications for the exhumation of (ultra-) high-pressure units. *Journal of Geodynamics*, 37(1), 1–55. https://doi.org/10.1016/j.jog.2003.10.001

Lardeaux, J. M., Caron J. M., Nisio P., Pequignot G., Boudelle M. (1986). Microstructural criteria for reliable thermometry in low-temperature eclogites. Lithos, 19(3–4), 187–203. https://doi.org/10.1016/0024-4937(86)90022-8

Li, Z. H., Liu M., Gerya T. (2016). Lithosphere delamination in continental collisional orogens: A systematic numerical study. *Journal of Geophysical Research: Solid Earth*, 121(7), 5186–5211. https://doi.org/10.1002/2016JB013106

Macente, A., Fusseis, F., Menegon, L., Xiao, X. John, T. (2017). The strain-dependent spatial evolution of garnet in a high-P ductile shear zone from the Western Gneiss Region (Norway): a synchrotron X-ray microtomography study. *Journal of Metamorphic Geology*, 35(5), 565–583. https://doi.org/10.1111/jmg.12245

Mainprice, D., Bascou, J., Cordier, P., Tommasi, A. (2004). Crystal preferred orientations of garnet: comparison between numerical simulations and electron back-scattered diffraction (EBSD) measurements in naturally deformed eclogites. *Journal of Structural Geology*, 26(11), 2089–2102. https://doi.org/10.1016/j.jsg.2004.04.008

Massey, M. A., Prior, D. J., Moecher, D. P. (2011). Microstructure and crystallographic preferred orientation of polycrystalline microgarnet aggregates developed during progressive creep, recovery, and grain boundary sliding *Journal of Structural Geology*, 33(4), 713–730. https://doi.org/10.1016/j.jsg.2010.12.009

Mauler, A., Godard, G. & Kunze, K. (2001). Crystallographic fabrics of omphacite, rutile and quartz in Vende´e eclogite (Armorican Massif, France): Consequences for deformation mechanisms and regimes. *Tectonophysics*, 342(1–2), 81–112. https://doi.org/10.1016/S0040-1951(01)00157-3

Menegon, L., Pennacchioni, G., Malaspina, N., Harris, K., Wood, E., 2017. Earthquakes as precursors of ductile shear zones in the dry and strong Lower Crust. *Geochemistry, Geophysics, Geosystems*, 18(12), 4356–4374. https://doi.org/10.1002/2017GC007189

Miladinova, I., Froitzheim, N., Nagel, T. J., Janák, M., Fonseca, R. O. C., Sprung, P., & Münker, C. (2022). Constraining the process of intracontinental subduction in the Austroalpine Nappes: Implications from petrology and Lu-Hf geochronology of eclogites. *Journal of Metamorphic Geology*, 40(3), 423–456. https://doi.org/10.1111/jmg.12634

Miller, C., & Thöni, M. (1997). Eo-Alpine eclogitisation of Permian MORB-type gabbros in the Koralpe (Eastern Alps, Austria): New geochronological, geochemical and petrological data. *Chemical Geology*, 137(3–4), 283–310. https://doi.org/10.1016/s0009-2541(96)00165-9

Moghadam, R. H., Trepmann, C. A., Stöckhert, B., & Renner, J. (2010). Rheology of Synthetic Omphacite Aggregates at High Pressure and High Temperature. *Journal of Petrology*, 51(4), 921–945. https://doi.org/10.1093/petrology/egq006

Petley-Ragan, A., Ben-Zion, Y., Austrheim, H., Ildefonse, B., Renard, F., & Jamtveit, B. (2019). Dynamic earthquake rupture in the lower crust. *Science Advances*, 5(7), eaaw0913. https://doi.org/10.1126/sciadv.aaw0913

Phillips, N. J., Ji, S. (2021). Constraining the ductile deformation mechanisms of garnet across pressure-temperature space. *Journal of Structural Geology*, 148, 104356 https://doi.org/10.1016/j.jsg.2021.104356

Philippot, P., & van Roermund, H. L. (1992). Deformation processes in eclogitic rocks: Evidence for the rheological delamination of the oceanic crust in deeper levels of subduction zones. *Journal of Structural Geology*, 14(8–9), 1059–1077. https://doi.org/10.1016/0191-8141(92)90036-v

Piepenbreier, D., & Stöckhert, B. (2001). Plastic flow of omphacite in eclogites at temperatures below 500°C – Implications for interpolate coupling in subduction zones. *International Journal of Earth Sciences*, 90(1), 197–210. https://doi.org/10.1007/s005310000159

Prior, D. J., Wheeler, J., Brenker, F. E., Harte, B. & Matthews, M. (2000). Crystal plasticity of natural garnet: new microstructural evidence. *Geology*, 28(11), 1003–1006. https://doi.org/10.1130/0091-7613(2000)28<1003:CPONGN>2.0.CO;2

Prior, D. J., Wheeler, J., Peruzzo, L., Spiess, R., Storey, C. (2002). Some garnet microstructures: an illustration of the potential of orientation maps and misorientation analysis in microstructural studies. *Journal of Structural Geology*, 24(6–7), 999–1011. https://doi.org/10.1016/S0191-8141(01)00087-6

Putnis, A., Austrheim, H., (2010). Fluid-induced processes: Metasomatism and metamorphism. *Geofluids*, 10(1–2), 254–269. https://doi.org/10.1111/j.1468-8123.2010.00285.x

Rast, M., Ruh, J. B. (2021). Numerical shear experiments of quartz-biotite aggregates: Insights on strain weakening and two-phase flow laws. *Journal of Structural Geology*, 149, 104375. https://doi.org/10.1016/j.jsg.2021.104375

Reuss, A., (1929). Berechnung der Fließgrenze von Mischkristallen auf Grund der Plastizitätsbedingung für Einkristalle. *Journal of Applied Mathematics and Mechanics*, 9(1), 49–58. https://doi.org/10.1002/zamm.19290090104

van Roermund, H. L. M. (1983). Petrofabics and microstructures of omphacites in a high temperature eclogite from the Swedish Caledonides. *Bulletin of Mineralogy*, 106(6), 709–713. https://doi.org/10.3406/bulmi.1983.7691

Rogowitz, A., & Huet, B. (2021). Evolution of fluid pathways during eclogitization and their impact on formation and deformation of eclogite: A microstructural and petrological investigation at the type locality (Koralpe, Eastern Alps, Austria). *Tectonophysics*, 819, 229079. https://doi.org/10.1016/j.tecto.2021.229079

Rogowitz, A., Thielmann, M., Kraus, K., Grasemann, B., & Renner, J. (2023). The effect of the garnet content on deformation mechanisms and weakening of eclogite: Insights from deformation experiments and numerical simulations. *Geochemistry, Geophysics, Geosystems*, 24, e2022GC010743. https://doi.org/10.1029/2022GC010743

Rutter, E. H. (1972). The influence of interstitial water on the rheological behaviour of calcite rocks. *Tectonophysics*, 14(1), 13–33. https://doi.org/10.1016/0040-1951(72)90003-0

Rybacki, E., Renner, J., Konrad, K., Harbott, W., Rummel, F., & Stöckhert, B. (1998). A servohydraulically-controlled deformation apparatus for rock deformation under conditions of ultra-high pressure metamorphism. *Pure and Applied Geophysics*, 152(3), 579–606. https://doi.org/10.1007/s000240050168

Segall, P., & Simpson, C. (1986). Nucleation of ductile shear zones on dilatant fractures. *Geology*, 14(1), 56–59. https://doi.org/10.1130/0091-7613(1986)14<56:nodszo>2.0.co;2

Schindelin, J., Arganda-Carreras, I., Frise, E., Kaynig, V., Longair, M., Pietzsch, T., Preibisch, S., Rueden, C., Saalfeld, S., Schmid, B., Tinevez, J.Y., White, D. J., Hartenstein, V., Eliceiri, K., Tomancak, P., Cardona, A. (2012). Fiji: an open-source platform for biological-image analysis. *Nature Methods*, 9, 676–82. https://doi.org/10.1038/nmeth.2019

Schott, J., Brantley, S., Crerar, D., Guy, C., Borcsik, M., Willaime, C. (1989). Dissolution kinetics of strained calcite. *Geochimica et Cosmochimica Acta.* 53(2), 373–382. https://doi.org/10.1016/0016-7037(89)90389-X

Schulmann, K., Mlčoch, B., Melka, R. (1996). High-temperature microstructures and rheology of deformed granite, Erzgehirge, Bohemian Massif. *Journal of Structural Geology*, 18(6), 719–733. https://doi.org/10.1016/S0191-8141(96)80007-1

Smulikowski, K. (1964). An attempt at eclogite classification. *Bulletin de l'Académie polonaise des Sciences, Série des Sciences géologiques et géographiques*, 12(1), 27–33.

Stern, R. J., Gerya, T. (2018). Subduction initiation in nature and models: A review. *Tectonophysics*, 746, 173–198. https://doi.org/10.1016/j.tecto.2017.10.014

Stöckhert, B., & Renner, J. (1998). Rheology of crustal rocks at ultrahigh pressure. In *When continents collide: Geodynamics and geochemistry of ultrahigh-pressure rocks* (pp. 57–95). Springer. https://doi.org/10.1007/978-94-015-9050-1

Storey, C. D., Prior, D. J. (2005). Plastic Deformation and Recrystallization of Garnet: A Mechanism to Facilitate Diffusion Creep. *Journal of Petrology*, 46(12), 2593–2613. https://doi.org/10.1093/petrology/egi067

Stünitz, H., Neufeld, K., Heilbronner, R., Finstad, A.K., Konopasek, J., Mackenzie, J.R. (2020). Transformation weakening: diffusion creep in eclogites as a result of interaction of mineral reactions and deformation. *Journal of Structural Geology*. 139, 104129. https://doi.org/10.1016/j.jsg.2020.104129

Tasaka, M., Zimmerman, M. E., Kohlstedt, D. L., Stünitz, H., Heilbronner, R. (2017). Rheological weakening of olivine + orthopyroxene aggregates due to phase mixing: Part 2. Microstructural development. *Journal of Geophysical Research: Solid Earth*, 122(10), 7597–7612. https://doi.org/10.1002/2017JB014311

Terry, M. P., & Heidelbach, F. (2006). Deformation-enhanced metamorphic reactions and the rheology of high-pressure shear zones, Western Gneiss Region, Norway. *Journal of Metamorphic Geology*, 24(1), 3–18. https://doi.org/10.1111/j.1525-1314.2005.00618.x

Trepmann, C. A., & Stöckhert, B. (2002). Cataclastic deformation of garnet: A record of synseismic loading and postseismic creep. *Journal of Structural Geology*, 24(11), 1845–1856. https://doi.org/10.1016/s0191-8141(02)00004-4

Tschumperle, D. & Deriche, R. (2005) Vector-Valued Image Regularization with PDE's: A Common Framework for Different Applications. *IEEE Transactions on Pattern Analysis and Machine Intelligence*, 27(4), 506–517. https://doi.org/10.1109/TPAMI.2005.87

Tullis, T. E., Horowitz, F. G., & Tullis, J. (1991). Flow laws of polyphase aggregates from end-member flow laws. *Journal of Geophysical Research: Solid Earth*, 96(B5), 8081–8096. https://doi.org/10.1029/90jb02491

Voegelé, V., Cordier, P., Sautter, V., Sharp, T. G., Lardeaux, J. M., & Marques, F. O. (1998). Plastic deformation of silicate garnets: II. Deformation microstructures in natural samples. *Physics of the Earth and Planetary Interiors*, 108(4), 319–338. https://doi.org/10.1016/s0031-9201(98)00111-3

Voigt, W. (1928). *Lehrbuch der Kristallphysik*. Teubner Verlag, Leipzig.

Wassmann, S., St¨ockhert, B., (2013). Rheology of the plate interface – Dissolution precipitation creep in high pressure metamorphic rocks. *Tectonophysics*, 608, 1–29. https://doi.org/10.1016/j.tecto.2013.09.030

Whitney, D. L. & Evans, B.W. (2010). Abbreviations for names of rock-forming minerals. *American Mineralogist*, 95(1), 185‑187. https://doi.org/10.2138/am.2010.3371

Yamato, P., Duretz, T., & Angiboust, S. (2019). Brittle/ductile deformation of eclogites: Insights from numerical models. *Geochemistry, Geophysics, Geosystems*, 20(7), 3116–3133. https://doi.org/10.1029/2019gc008249

Zhang, J. & Green, H. W. (2007). Experimental investigation of eclogite rheology and its fabrics at high temperature and pressure. *Journal of metamorphic Geology*, 25(2), 97–115. https://doi.org/10.1111/j.1525-1314.2006.00684.x

Zhang, J. & Green, H. W. (2007). On the Deformation of UHP Eclogite: From Laboratory to Nature. *International Geology Review*, 49(6), 487–503. https://doi.org/10.2747/0020-6814.49.6.487

Zhang, J., Green, H. W., Bozhilov, K. N. (2006). Rheology of omphacite at high temperature and pressure and significance of its lattice preferred orientations. *Earth and Planetary Science Letters*, 246 (3–4), 432–443. https://doi.org/10.1016/j.epsl.2006.04.006

Zhang, J., Green, H. W., Bozhilov, K. N. & Jin, Z. M. (2004). Faulting induced by precipitation of water at grain boundaries in hot subducting oceanic crust. *Nature*, 428, 633–636. https://doi.org/10.1038/nature02475

APPENDIX

a. Experimental procedure protocol and summary table

Experiment setup and sample assembly construction

Synthesized samples were removed from their gold jacket by manually grinding them with sandpaper. They were then inserted into a new cylindrical gold jackets and sealed off mechanically with a thin gold disc and a 1 mm-thick ceramic plug on top. The sample assembly was then constructed on the base plate.

To construct the sample assembly, two thermocouples ('ABB type-K' – composed of Ni and Ni-Cr alloy) were guided into two holes through the bottom of the base plate. The thermocouples must protrude by exactly the height necessary to reach the bottom and the middle of the sample respectively. A punctured metal sleeve shielded by a pyrophyllite gasket was then positioned on the base plate, with the two thermocouples guided through its holes. Next, a ceramic pedestal was inserted into the metal sleeve. A three-layer tube, which includes an outer pyrophyllite layer, an inner salt (NaCl) layer, and an 'Inconel' (Ni-Cr alloy) sleeve in between, was placed on top of the metal sleeve, surrounding the ceramic pedestal. The 'Inconel' sleeve's function is to reduce the temperature gradient on the sample (S. Floreen & J. L. Nelson, 1983). The two thermocouples are terminating inside the wall of the pyrophyllite tube. Next, the gold jacket containing the sample was placed inside the inner tube. A thin graphite mantle (graphite resistance furnace) and an outer salt (NaCl) layer were then put on top of the metal sleeve, surrounding the pyrophyllite mantle. A thin layer of loose salt (~1.5 – 3 mm) was used to confine the sample over the ceramic plug.

The pressure vessel was positioned over the base plate with an insulating mica sheet in between the two plates. The deformation piston, which consists of a ceramic and a steel part glued together, was inserted into the inner salt sleeve with the ceramic part contacting the loose salt cover. Next, the sample assembly was sealed off with a graphite lid, which together with the graphite furnace and the metal sleeves form the electrical connection needed for heating, and a Fe-ring, which prevents molten metal from flowing into the assembly. An Sn-Al plug (Al in the case of sample PE03), which increases homogeneity in force distribution, was placed on top. Moreover, an Al-ring and two 'mitre' ('δ') rings (made of hardened steel) of different diameter were placed on top for further insulation. Finally, the confining piston was placed on top of the Sn-Al plug, with another insulating mica sheet in between the pressure vessel and the confining piston.

The entire construction, which includes the base plate, sample assembly and pressure vessel was then inserted into the Griggs deformation apparatus, and the heating and cooling systems were connected. Last, the end load ram of the deformation column was leveled down with a hydraulic pump, until contacting the top of the pressure vessel.

Heating/pressurizing phase

Before initializing the servohydraulics, the inside of the pressure vessel must be under some minimum amount of pressure, thus a hydraulic pump was used to build-up pressure up to ~ 1.5 MPa before enabling the servohydraulics.

The heating ramp which was implemented in all deformation experiments included a 10° C/min program for the first 300° C, slowing down to 5° C/min until the target confining temperature of 900° C. Upon reaching 100° C, the servohydraulically-controlled pressure build-up system was initialized, at a rate of 1 MPa/min up to 10 MPa. Upon reaching 10 MPa of oil pressure (which corresponds to ~ 317.9 MPa of confining pressure), the pressure build-up was halted, waiting for temperature to begin surpassing the 300° C mark before continuing to build-up more pressure; the final pressurizing ramp was slower (0.5 MPa/min), and was constantly applied until the target confining pressure of 2.5 GPa (78.62 MPa of oil pressure). During the entire pressure build-up procedure, it is important to be aware of the intensifier oil reservoir indicator; about twice in each experiment, the intensifier almost depletes (indicator reaches the top) and needs to be refilled with oil from the main oil reservoir; this is achieved by pumping via a hydraulic pump.

During the early heating/pressurizing phase (until ~500° C), friction between the metallic parts of the apparatus is significantly high, introducing tensional forces in the deformation column, which cause internal parts to separate from each other and the axial load to drop. This separation allows molten metal to infiltrate and take part in the deformation, thus altering the mechanical data. To prevent this, the recorded load was constantly monitored and the W50 LVDT's position was adjusted accordingly.

Deformation phase

Upon reaching the confining pressure/temperature conditions, the W5 LVDT was used to control the movement of the deformation piston. A constant strain rate of $6.4 \cdot 10^{-6}$ s^{-1} was applied, by implementing a velocity of 0.185 mm/h to the W5 LVDT (0.182 mm/h for PE03). The velocity of the deformation piston is calculated by the formula $V = SR * LS$ (V = velocity, SR = strain rate, L_S = sample length).

During the early deformation phase, the hit point was identified to calculate the remaining deformation time. The hit point is the moment the deformation piston encounters and begins deforming the sample and is identified by a change in curvature of the recorded load-time curve.

Cooling/depressurizing phase

After a sample was deformed up to the target degree of axial strain, the W5 LVDT was slowly driven to the opposite direction, relieving the sample from the σ_1 stress component. After the W5 LVDT was driven out of the sample assembly, a pressure/temperature decrease program was implemented. The cooling ramp applied included a 5° C/min temperature decrease up to 300° C, accelerating to 10° C/min until reaching room temperature. A slow pressure decrease program (0.5 MPa/min) was also applied. During decompression, the intensifier indicator was monitored because the reservoir is filling with oil from the chamber. When the reservoir approaches its full capacity, the tension valves had to be loosened to push the oil from the intensifier reservoir into the main oil reservoir, providing room for more oil flowing from the pressure vessel into the intensifier.

Retrieval of the deformed sample

Upon reaching room pressure/temperature conditions, the deformation column was driven back up, and the pressure vessel/base plate construction was removed from the apparatus. The samples were extracted from the pressure vessel using a hydraulic press and were submerged in hot water to dissolve the salt and other soluble parts. Finally, the gold jackets were manually ground off the sample's surface with fine sandpaper.

Table 5: All experimental details. The mechanical data from experiment 2 * (PE03) are unusable; there is no distinguishable hit point and the axial strain listed in the table is based on the measured physical axial shortening of the recovered sample. Axial strain values for experiment 1 and 3 (PE02, PE04) were derived from the corrected stress versus strain curves shown in Figure 8.

	Experiment 1	**Experiment 2 ***	**Experiment 3**
Sample №	**PE02**	**PE03**	**PE04**
Deformation piston velocity (mm/h)	0.185	0.182	0.185
Duration (h)	42.5	23.0	44.0
Hit point	Load: -66.1 kN W5: -0.4 mm	–	Load: -57.6 kN W5: -1.17 mm
Maximum load	Load: -76.59 kN W5: 0.35 mm	Load: -86 kN W5: 0.1 mm	-63.6 kN W5: -6.02 mm
Confining pressure ramp	1 MPa/min →10 MPa 0,5 MPa/min →78 MPa	1 MPa/min →10 MPa 0,5 MPa/min →78 MPa	1 MPa/min →10 MPa 0,5 MPa/min →78 MPa
Confining temperature ramp	10° C/min → 300° C 5° C/min → 900° C	10° C/min → 300° C 5° C/min → 900° C	10° C/min → 300° C 5° C/min → 900° C
Deformation start (time/date)	21:21 12.11.19	18:26 14.11.19	18:45 18.11.19
Deformation stop (time/date)	21:58 13.11.19	13:22 15.11.19	12:29 19:11.19
Deformation duration (h: min)	24:37	18:56	17:44
Sample length before (mm)	8.05	7.88	8.04
Sample diameter before (mm)	3.39	3.37	3.44
Sample length before with Au (mm)	9.78	9.42	9.93
Sample length after (mm)	7.38	3.89	7.05
Sample length after with Au (mm)	8.89	8.69	9.14
Sample diameter after with Au (mm)	3.03 – 2.93	3.4 – 3.36	2.89 – 2.87
Axial strain (%)	**~7%**	**~42% ***	**~4.7%**

b. Mechanical data corrections

A Matlab® script was used to carry out the system friction and stiffness corrections. First, the array of displacement values, measured by the W5 LVDT, was divided by the sample's length before deformation to acquire unfiltered axial strain values. Furthermore, the array of load values, measured by the external load cell, was multiplied by the surface ratio between the ram and the confining piston to acquire unfiltered axial stress values. Next, the unfiltered stress-strain curve was plotted. The slope of the unloading segment is assumed to represent the stiffness of the internal parts of the apparatus; thus, it was used to filter-out the effect of internal friction on the mechanical data. Accordingly, the unfiltered axial strain values were divided by the slope coefficient of the unloading segment, to acquire true axial strain values. Nominal uncertainty in axial strain is ~0.1%, considering the accuracy of the W5 LVDT's displacement measurement, and the uncertainty in stiffness correction (Moghadam et al., 2010).

Next, to filter-out the effects of internal friction of the apparatus, another stress vs. strain graph was plotted using the computed true strain values. From this plot, the hit point was graphically determined as the intersection of the two trend lines for dynamic friction and elastic deformation of the sample. The slope of the dynamic friction part of the curve is assumed to represent the internal friction of the apparatus; thus the slope coefficient was computed and subtracted from the unfiltered axial stress values to acquire true differential stress values ($\Delta\sigma$). The uncertainty in true axial differential stress values is estimated at $\pm$ 0.2 GPa, considering the uncertainties in the accuracy of the external load cell, sample diameter measurement, and the uncertainty in friction correction (Druiventak et al., 2011).

The resulting strain-stress curves were confined to the range of values representing actual sample deformation and were smoothed-out by a moving average filter (with a span of 0.5). Figure 25 displays the unfiltered load-displacement curves of samples PE02 and PE04. The hit point, which indicates the onset of sample deformation, as well as the dynamic friction and unloading segments are marked.

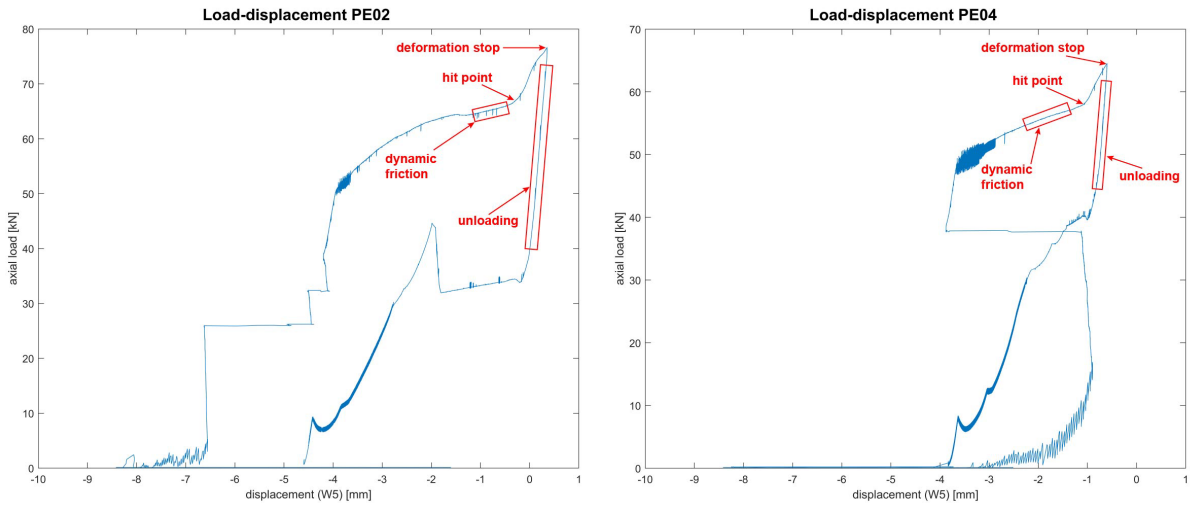

Figure 25: Unfiltered load-displacement curve of samples PE02 and PE04. The hit point, dynamic friction and unloading segments are marked.

c. 3D data processing settings

2D Anisotropic Diffusion Filter plug-in (Fiji®) settings:

- Number of iterations: 13.
- Smoothings per iteration: 1.
- A1: 0.4 (diffusion limiter for low gradients – lower values reduce noise).
- A2: 0.9 (diffusion limiter for high gradients – higher values preserve more edges).
- Dt (time step): 20.
- Edge threshold height: 4 (lower values preserve more edges).

Trainable Weka Segmentation 3D plug-in (Fiji®) settings:

radius (σ) of 1 to 8 voxels around the target pixel for all implemented operations:

- Mean smoothing operation.
- Variance smoothing operation.
- Gaussian blur operation (this applies several convolutions using a Gaussian function to the neighboring voxels).

Avizo® settings:

- Border kill operator: neighborhood: 26 (voxels with at least one common vertex with the model's margins are excluded)
- Erosion operator: neighborhood: 6 (voxels with a at least one exposed face are eroded); half-kernel size: 3 pixels.
- Volume rendering operator: lighting: diffuse, deferred; shade effects: ambient; interpolation: cubic; gradient: normal; global illumination: ambient occlusion; sampling quality: 2.

Quant3D settings:

- Volume of interest (VOI): centered sphere; use VOI for threshold calculation.
- Threshold method (user entered value): 242 – 255 for both phases.
- Orientations: 2049 uniform orientations with random rotation and dense vectors.
- Statistics: 5000 Points; omit side-intersecting paths (this excludes intercepts exiting the VOI).

d. Microtomographic data sets and visualizations of the modeled garnet volumes

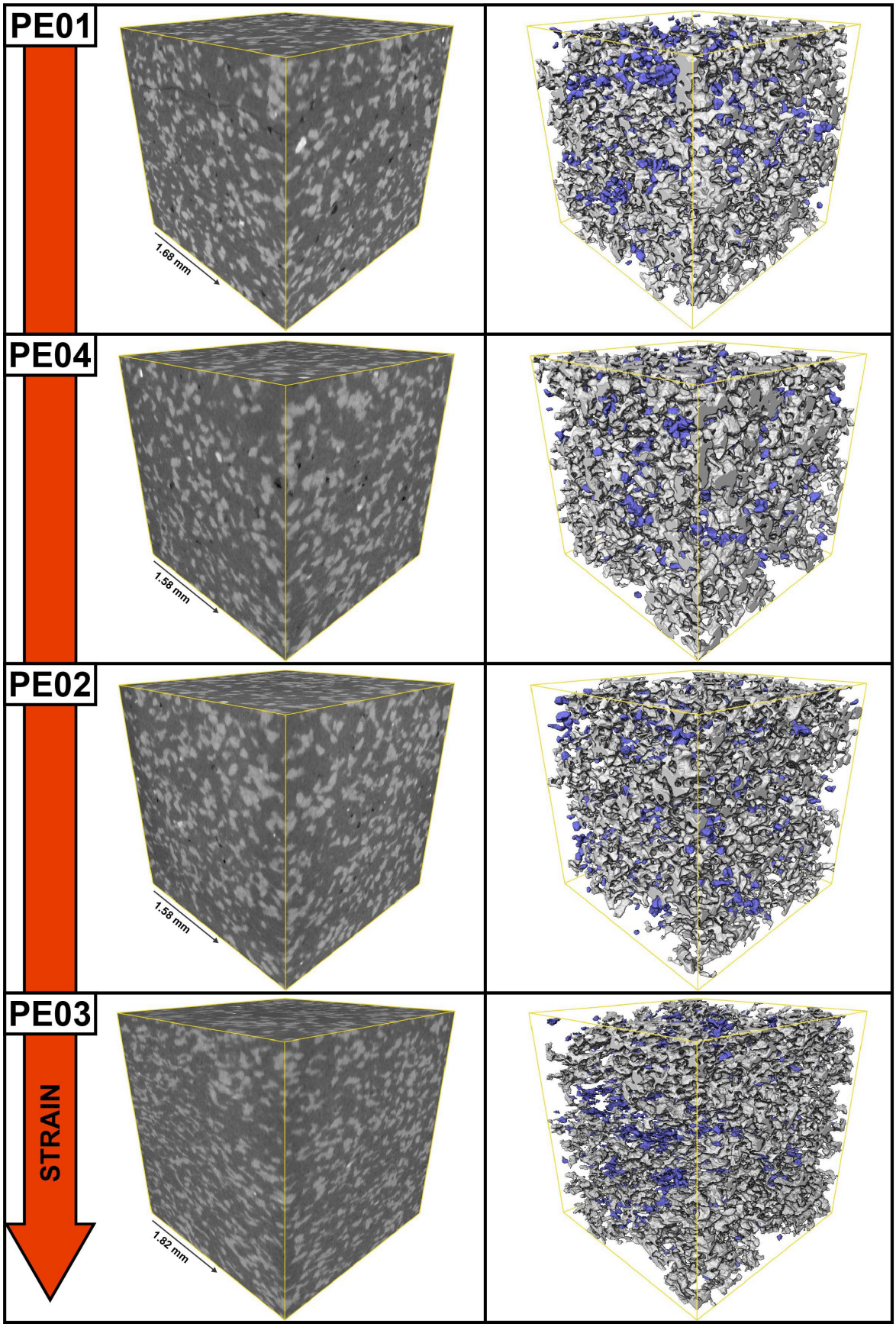

Figure 26: Left: Microtomographic data sets. Right: Volume renderings of the eroded interconnected and isolated garnet clusters.

Appendix References

Druiventak, A., Trepmann, C. A., Renner, J., and Hanke, K. (2011). Low-temperature plasticity of olivine during high stress deformation of peridotite at lithospheric conditions - An experimental study. *Earth and Planetary Science Letters*, 311(3–4), 199–211. https://doi.org/10.1016/j.epsl.2011.09.022

Floreen, S., Nelson, J. L. (1983). The effects of heat treatment and composition on the stress corrosion cracking resistance of inconel alloy X-750. *Metallurgical and Material Transactions A*, 14, 133–139. https://doi.org/10.1007/BF02643746

Moghadam, R. H., Trepmann, C. A., Stöckhert, B., and Renner, J. (2010). Rheology of Synthetic Omphacite Aggregates at High Pressure and High Temperature. *Journal of Petrology*, 51(4), 921–945. https://doi.org/10.1093/petrology/egq006